Cell Reports
Medicine

Article

High NEK2 expression in myeloid progenitors suppresses T cell immunity in multiple myeloma

Graphical abstract

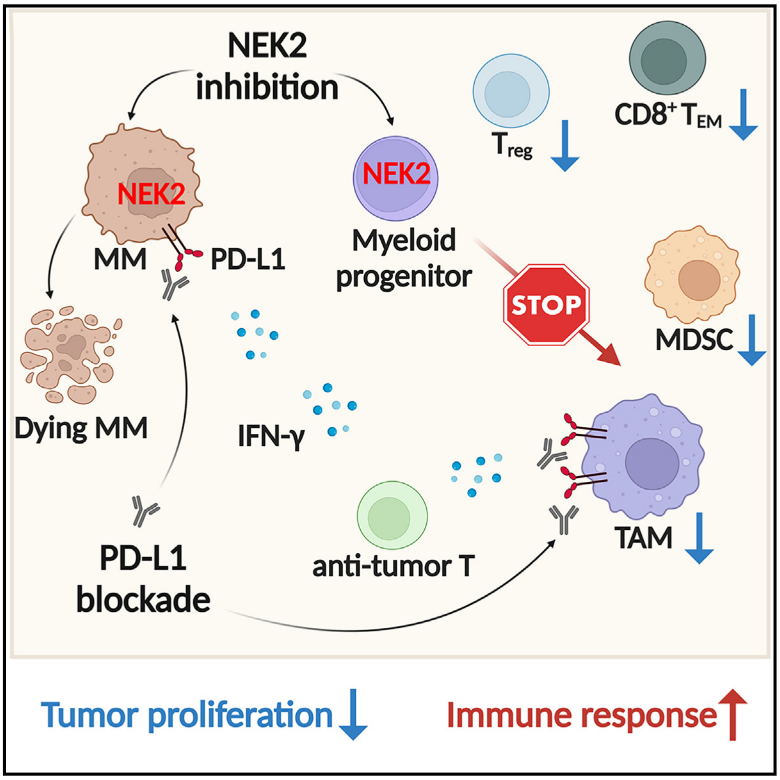

Highlights

- Loss of NEK2 in tumor microenvironment suppresses MM cell growth
- High NEK2 expression induces polarization of myeloid progenitors to TAMs
- Low NEK2 expression is linked to an increased IFN-γ gene signature in MM cells
- NEK2 inhibitor INH154 sensitizes MM cells to PD-L1 blockade

Authors

Yan Cheng, Fumou Sun,
Daisy V. Alapat, ..., Guido Tricot,
John D. Shaughnessy, Jr.,
Fenghuang Zhan

Correspondence

fzhan@uams.edu

In brief

Cheng et al. demonstrate a mechanism of immune suppression regulated by NEK2 in an MM mouse model. Clinically, low NEK2 with high PD-L1 expression predicts a longer survival. Combining the NEK2 inhibitor INH154 with PD-L1 blockade effectively eliminates MM cells in mice.

Cheng et al., 2023, Cell Reports Medicine *4*, 101214
October 17, 2023 © 2023 The Authors.
https://doi.org/10.1016/j.xcrm.2023.101214

CellPress

Cell Reports Medicine

CellPress
OPEN ACCESS

Article

High NEK2 expression in myeloid progenitors suppresses T cell immunity in multiple myeloma

Yan Cheng,[1,10] Fumou Sun,[1,10] Daisy V. Alapat,[2] Visanu Wanchai,[1,3] David Mery,[1] Wancheng Guo,[1] Huojun Cao,[4] Yuqi Zhu,[5] Cody Ashby,[3] Michael Anton Bauer,[3] Intawat Nookaew,[3] Eric R. Siegel,[6] Jun Ying,[6] Jin-Ran Chen,[7] Dongzheng Gai,[1] Bailu Peng,[1] Hongwei Xu,[1] Clyde Bailey,[1] Samer Al Hadidi,[1] Carolina Schinke,[1] Sharmilan Thanendrarajan,[1] Maurizio Zangari,[1] Marta Chesi,[8] P. Leif Bergsagel,[8] Frits van Rhee,[1] Siegfried Janz,[9] Guido Tricot,[1] John D. Shaughnessy, Jr.,[1] and Fenghuang Zhan[1,11,*]

[1]Myeloma Center, Winthrop P. Rockefeller Institute, Department of Internal Medicine, University of Arkansas for Medical Sciences, Little Rock, AR 72205, USA
[2]Department of Pathology, College of Medicine, University of Arkansas for Medical Sciences, Little Rock, AR 72205, USA
[3]Department of Biomedical Informatics, College of Medicine, University of Arkansas for Medical Sciences, Little Rock, AR 72205, USA
[4]Iowa Institute for Oral Health Research, Division of Biostatistics and Computational Biology, Department of Endodontics, University of Iowa College of Dentistry, Iowa City, IA 52242, USA
[5]Department of Internal Medicine, University of Iowa, Iowa City, IA 52242, USA
[6]Department of Biostatistics, University of Arkansas for Medical Sciences, Little Rock, AR 72205, USA
[7]Arkansas Children's Nutrition Center, University of Arkansas for Medical Sciences, Little Rock, AR 72202, USA
[8]Department of Hematology/Oncology, Mayo Clinic, Scottsdale, AZ 85259, USA
[9]Division of Hematology and Oncology, Department of Medicine, Medical College of Wisconsin, Milwaukee, WI 53226, USA
[10]These authors contributed equally
[11]Lead contact
*Correspondence: fzhan@uams.edu

https://doi.org/10.1016/j.xcrm.2023.101214

SUMMARY

Multiple myeloma (MM) growth is supported by an immune-tolerant bone marrow microenvironment. Here, we find that loss of Never in mitosis gene A (NIMA)-related kinase 2 (NEK2) in tumor microenvironmental cells is associated with MM growth suppression. The absence of NEK2 leads to both fewer tumor-associated macrophages (TAMs) and inhibitory T cells. NEK2 expression in myeloid progenitor cells promotes the generation of functional TAMs when stimulated with MM conditional medium. Clinically, high NEK2 expression in MM cells is associated with increased $CD8^+$ T effector memory cells, while low NEK2 is associated with an IFN-γ gene signature and activated T cell response. Inhibition of NEK2 upregulates PD-L1 expression in MM cells and myeloid cells. In a mouse model, the combination of NEK2 inhibitor INH154 with PD-L1 blockade effectively eliminates MM cells and prolongs survival. Our results provide strong evidence that NEK2 inhibition may overcome tumor immune escape and support its further clinical development.

INTRODUCTION

Multiple myeloma (MM) is characterized by malignant plasma cells accumulating in the bone marrow (BM), typically with high levels of monoclonal protein detected in the peripheral blood, causing "CRAB" clinical symptoms including hypercalcemia, renal injury, anemia, and bone lesions.[1] Advances in MM therapy with the use of immunomodulatory drugs, proteasome inhibitors, and monoclonal antibodies (mAbs) along with high-dose chemotherapy and autologous stem cell support have improved overall 5-year survival from 35% to 50% over the past 20 years. However, high-risk (HR) and relapsed or refractory (RR) MM remain largely incurable. The observation of durable remissions after allogeneic stem cell transplantation, possibly caused by graft-versus-myeloma effects,[2–4] and the growing success of CAR-T therapy[5–8] suggest that surveillance and cytotoxic ability of activated T cells are critical for tumor eradication and maintenance of durable remissions. However, cancer-induced changes in T cell composition and dysfunction of cytotoxic T cells have been observed in MM leading to tumor immune escape and resistance to immunotherapies.[9,10] Such T cells have reduced proliferative capacity, decreased interferon γ (IFN-γ) secretion, and are characterized by expression of inhibitory receptors, such as PD1 and TIGIT.[11] They are frequently observed in an effector memory (T_{EM}) or terminally differentiated (T_{EMRA}) status, which is TCF1 negative and lacks stem cell-like properties, largely due to chronic antigen exposure.[12] How T cell function is being dynamically manipulated in the MM BM microenvironment is still incompletely understood.

The BM microenvironment contains immune cells at various stages of differentiation. Growing evidence shows that tumor-associated macrophages (TAMs) and myeloid-derived suppressor cells (MDSCs) are key players of innate immunity suppressing anti-MM T cell responses.[13–15] Macrophages are derived from the monocyte lineage and play a crucial role in maintaining tissue homeostasis, defense against pathogens, and wound healing. TAMs exhibit a unique phenotype with increased secretion of interleukin 1β (IL-1β), IL-6, IL-10, and expression of CD163 and CD206 that are shaped by the tumor microenvironment.[16] MDSCs have been identified as a new group of myeloid cells with potent immune suppressive function. Depending on their surface phenotype, MDSCs can be further divided into granulocytic MDSCs (G-MDSCs) or monocytic MDSCs (Mo-MDSCs). Both TAMs and MDSCs express high levels of arginase 1 (ARG1), a well-characterized marker of immunosuppressive myeloid cells.[17,18] Recent studies report that antibodies targeting immune checkpoints with enhanced Fc-gamma receptor (FcγR)-engagement activity exhibit a strikingly enhanced antitumor function.[19,20] These findings highlight that innate-like T cell phenotypes or myeloid activation represent potential therapeutic targets to restore antitumor T cell responses.

Our previous studies have identified that HR and RR MM cells express high levels of chromosomal instability (CIN) genes.[21] Associated with copy number amplification of chromosome 1q, elevated expression of Never in mitosis gene A (NIMA)-related kinase 2 (NEK2) in MM cells is strongly associated with inferior survival and drug resistance in MM.[21,22] NEK2 is a serine-threonine kinase belonging to the NEK family of NIMA proteins that regulate cell mitosis.[23] B cell-specific overexpression of NEK2 in transgenic mice regulates B cell development and enhances T cell-dependent immune responses.[24] NEK2 suppresses immune effector cells by stabilizing PD-L1 expression.[25] However, little is known about NEK2 in regulating MM immunity. Systemic agents targeting NEK2 expression in tumor cells are being developed.[26] Whether suppressing NEK2 in the BM microenvironment will have added clinical benefit is not known. In this study, we have investigated the role of NEK2 inhibition in the MM immune microenvironment and have assessed the potential therapeutic benefits of systemic NEK2 inhibition in MM.

RESULTS

Knockout of NEK2 improves Eμ-*myc* mouse survival and induces T cell activation

NEK2 overexpression in the B cell lineage affects B cell development.[24] To determine whether deficiency of NEK2 inhibits B cell malignancies, we generated *Nek2*$^{-/-}$ mice (Figures S1A–S1C). Next, we crossed *Nek2*$^{-/-}$ mice with Eμ-*myc* transgenic mice, a well-established Myc-driven preclinical model for B cell malignancies. Eμ-*myc/Nek2*$^{+/+}$ and Eμ-*myc/Nek2*$^{+/-}$ mice showed similar survival (Figure 1A). However, Eμ-*myc/NEK2*$^{-/-}$ mice had significantly prolonged survival (Figure 1A), indicating that loss of both alleles of NEK2 delays B cell lymphoma progression. To study the early stages of B cell tumor development in these mice, we collected blood, BM, and spleen samples when mice were 6–8 weeks old. Complete blood count analysis showed that Eμ-*myc/Nek2*$^{-/-}$ mice had decreased numbers of circulating lymphocytes and increased platelets when compared with Eμ-*myc/Nek2*$^{+/+}$ mice (Figure 1B). Decreased weights of the spleen and thymus were also observed (Figure 1C). Flow cytometry of B cell subsets of BM and spleen further identified that, when compared with *Nek2*$^{+/+}$ mice, Eμ-*myc/Nek2*$^{+/+}$ mice had increased pre- and pro-B but decreased mature B cells, while Eμ-*myc/Nek2*$^{-/-}$ mice had reduced pre- and pro-B cells but a less pronounced loss of mature B cells (Figures 1D and S1D). Hence, loss of NEK2 limits Myc-induced lymphomagenesis.

To characterize the transcriptome of Eμ-*myc/Nek2*$^{-/-}$ mice compared with Eμ-*myc/Nek2*$^{+/+}$ mice, we collected pre-malignant B cells and performed RNA sequencing (Figure 1E). Mitotic and cell-cycle-related pathways were significantly downregulated in Eμ-*myc/Nek2*$^{-/-}$ mice (Figure S1E). Interestingly, immune-related pathways were significantly upregulated (Figures 1F and S1F; Table S1), strongly suggesting that lack of NEK2 is associated with immune activation. Next, we selected cell membrane genes and secreted genes associated with immune regulation and cell trafficking based on GO annotation (Figure S1G). *Cxcl9*, which is critical in antitumor immunity and dependent on the production of IFN-γ,[27] had the highest fold change (log2FC = 10.5). Several inhibitory immune receptors were also upregulated, including *Cd274* (encoding PD-L1). To test if upregulation of PD-L1 was due to the activation of IFN-γ, we analyzed the downstream targets of the IFN-γ signal in the mouse B cells. JAK/STAT1/IRF1 signaling showed a significant activation in Eμ-*myc/Nek2*$^{-/-}$ mice when compared with Eμ-*myc/Nek2*$^{+/+}$ mice (Figures 1G and 1H). NEK2 was expressed abundantly in BM myeloid cells (CD11b$^+$) and T cells (CD3$^+$) (Figure S1H), suggesting that loss of NEK2 in the microenvironment may affect immune surveillance in B cell malignancies. Finally, to determine the activation status of T cells from tumor-bearing and nontumor-bearing *Nek2*$^{+/+}$ and *Nek2*$^{-/-}$ mice, we performed flow cytometry. CD8$^+$ naive T cells (T_N) were suppressed in Eμ-*myc/Nek2*$^{+/+}$ mice when compared with mice without tumors, but this loss was not observed in Eμ-*myc/Nek2*$^{-/-}$ mice (Figures 1I and S1I). On the other hand, CD8$^+$ T_{EM} showed the opposite picture (Figures 1I and S1I). However, PD1 expression on T cells was not significantly changed. These data suggest that T cell responses are less driven toward an effector memory phenotype in Eμ-*myc* mice with NEK2 knockout and that improved T cell immune responses against Myc-induced B cell malignancies exist.

Loss of NEK2 reduces tumor-associated macrophages and Tregs

To determine how the lack of NEK2 in the tumor microenvironmental cells contributes to tumor inhibition and immune regulation, we tested the growth of 5TGM1 MM cells in *Nek2*$^{-/-}$ mice compared with their *Nek2*$^{+/+}$ littermates (Figure 2A). Inoculation of 5TGM1 MM cells in the *Nek2*$^{-/-}$ mice resulted in lower serum IgG2b levels and longer survival (Figures 2B and 2C). Single-cell RNA sequencing (scRNA-seq) was employed to survey the cellular diversity and the transcriptome of BM cells. Using standard quantity controls, we analyzed a total of 30,284 BM cells. Projecting cells onto a 2D Uniform Manifold Approximation and Projection (UMAP) plot, we found 17 distinct cell clusters

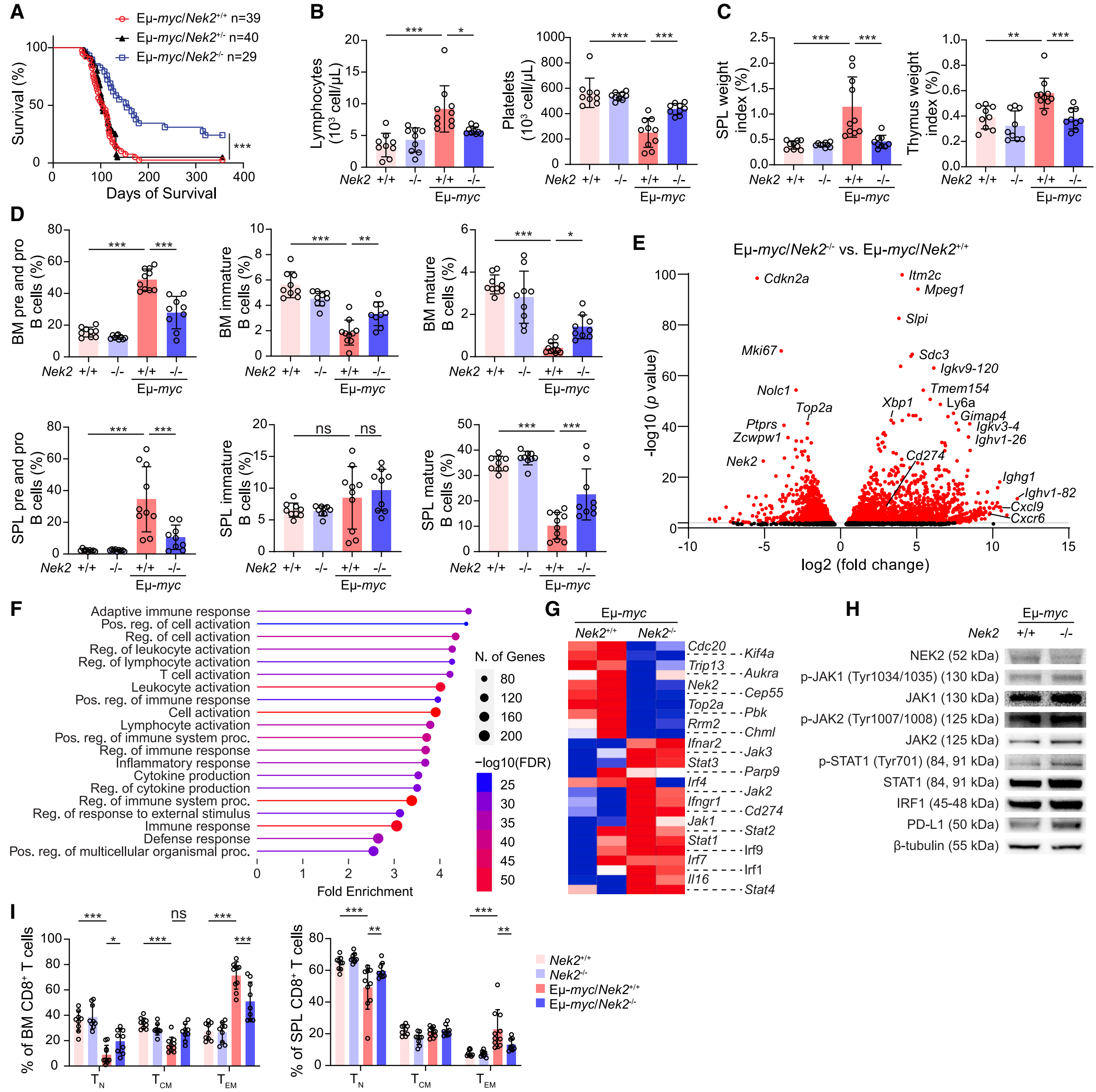

Figure 1. Knockout of NEK2 improves Eμ-*myc* mouse survival and induces T cell activation

(A) Overall survival of Eμ-*myc* mice with indicated *Nek2* genotypes.

(B–D) Numbers of circulating lymphocytes and platelets in peripheral blood (B); spleen (SPL) and thymus weight index as calculated by normalizing to body weight (C); flow cytometry analyses of percentages of pre- and pro-B cells ($B220^{low}IgM^{-}$), immature B cells ($B220^{low}IgM^{+}$), and mature B cells ($B220^{high}IgM^{+}$) from bone marrow (BM) and SPL (D) in indicated groups. n = 9–10 mice/group from three independent experiments. Boxplot shows mean ± SD and the p value for the two-way ANOVA followed by Sidak multiple comparison test.

(E–G) Volcano plot showing differential gene expression, where red dots represent genes with a $|\log2FC| > 2$ and p value <0.01 (E); Gene Ontology (GO) analysis of upregulated genes (F); and heatmap showing gene expression level of selected chromosomal instability genes and IFN-γ signature genes (G) in $CD19^{+}$ SPL cells of Eμ-*myc/Nek2*$^{-/-}$ vs. Eμ-*myc/Nek2*$^{+/+}$ mice. n = 2 mice/group.

(H) Western blot analysis of cell lysates to detect JAK/STAT1/IRF1/PD-L1 pathway in $CD19^{+}$ SPL cells of Eμ-*myc/Nek2*$^{-/-}$ vs. Eμ-*myc/Nek2*$^{+/+}$ mice.

(I) Flow cytometry analyses showing percentages of T naive cells (T_N, $CD62L^{+}CD44^{-}$), T central memory (T_{CM}, $CD62L^{+}CD44^{+}$), and T effector memory (T_{EM}, $CD62L^{-}CD44^{+}$) of $CD8^{+}$ T cells from BM and SPL in indicated groups. n = 9–10 mice/group from three independent experiments. Boxplot shows mean ± SD and the p value for the two-way ANOVA followed by Sidak multiple comparison test. ns, $p > 0.05$; *$p < 0.05$; **$p < 0.01$; ***$p < 0.001$. Please also see Figure S1 and Table S1.

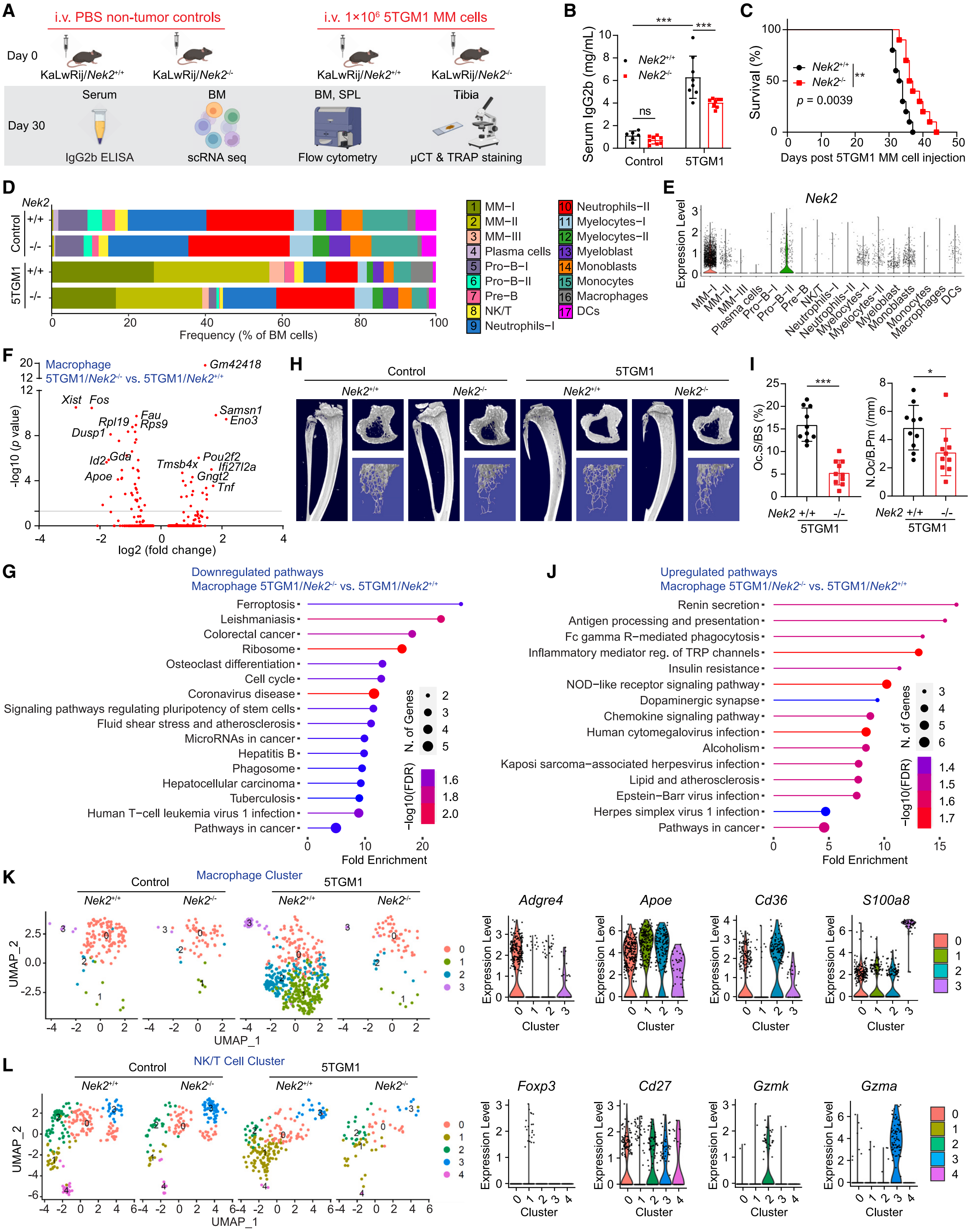

(legend on next page)

(Figures 2D, S2A, and S2B; Table S2). The 5TGM1 MM cells were identified by their high expression of *Sdc1* (encoding CD138) and appeared only in the 5TGM1 injected mice. Consistent with tumor burden, as measured by mouse serum IgG2b levels, scRNA-seq showed that the 5TGM1/*Nek2*$^{-/-}$ group (~40%) had lower percentages of MM cells in the BM compared to the 5TGM1/Nek2$^{+/+}$ group (~60%) (Figure 2D). Normal plasma cells and pro-B cells clusters were strikingly decreased in mice with 5TGM1 MM cell injections, indicating a defect of normal B cell development in the presence of MM. This concurs with a recent report that MM patients showed a decreased normal plasma cell percentage using scRNA-seq.[28] However, the loss of pro-B cells was partially restored in 5TGM1/*Nek2*$^{-/-}$ mice compared to 5TGM1/*Nek2*$^{+/+}$ mice (Figure S2B). Myeloid cells were the most abundant immune cells within the BM. Macrophage clusters increased 3.6-fold in the tumor-bearing *Nek2*$^{+/+}$ mice compared with *Nek2*$^{+/+}$ mice. However, among the tumor-bearing mice, *Nek2*$^{-/-}$ mice had 87% fewer macrophages compared with the *Nek2*$^{+/+}$ mice (Figure S2B).

One interesting finding is that besides MM cells and pro-B cells, NEK2 was most abundantly expressed in the myelocyte and monoblast clusters (Figure 2E). This finding is supported by scRNA-seq data from other studies[29] (Figure S2C). To identify differentially expressed genes in the macrophage clusters between 5TGM1/Nek2$^{+/+}$ and 5TGM1/*Nek2*$^{-/-}$ groups, a total of 56 upregulated and 43 downregulated genes were identified (Figure 2F). KEGG pathway analysis revealed that *Ferroptosis*, *Osteoclast differentiation,* and *Cell cycle* were decreased in 5TGM1/*Nek2*$^{-/-}$ macrophages (Figure 2G). We observed decreased bone lesions on microcomputed tomography (μCT) (Figures 2H and S2D) and decreased numbers of osteoclasts in the tibia on TRAP staining in 5TGM1/*Nek2*$^{-/-}$ compared with 5TGM1/*Nek2*$^{+/+}$ mice (Figures 2I and S2E). 5TGM1/*Nek2*$^{-/-}$ macrophages exhibited positive enrichment for *Antigen processing and presentation*, *Fc gamma R-mediated phagocytosis*, *NOD-like receptor signaling pathway*, and *chemokine signaling pathway* (Figure 2J). To further analyze phenotypic differences in macrophages among the groups, a total of 740 macrophages were projected onto a UMAP plot based on the expression of highly variable genes, and four subpopulations of macrophages were identified (Figure 2K). Subpopulation M-1 (*Cirbp*, *Nfil3*, *Mt1*, *Apoe*), M-2 (*CD36, Bcl2a1b*), and M-3 (*S100a9*, *S100a8, Lcn2*) mainly appeared in the tumor-bearing group, while these genes were suppressed in 5TGM1/*Nek2*$^{-/-}$ group, which was characterized by genes related to immune suppression (*Apoe, S100a9, S100a8*), macrophage deactivation (*Lcn2*), and anti-apoptosis (*Bcl2a1b*) (Figure 1K). The M-0 (*Cd74*, *Ace*, *Adgre4*) subpopulation, characterized by genes related to antigen presentation (*Cd74*), macrophage activation (*Adgre4*, *Adgre5*), and chemotaxis (*Ccr2*, *Csf1r*, *Cx3cr1*) (Figure 2K) remained unchanged across all groups. NK/T cell cluster comparison (a total of 627 cells) showed a dramatic increase in the T-1 (*CD4*, *Foxp3*, *Ctla4*) subpopulation, which was characterized by genes related to exhaustion (*Foxp3, Ctla4*) and loss of T cell activating markers (*CD27, Gzmk, Gzma*) (Figure 2L), indicating that T regulatory cells (Tregs) were increased in 5TGM1/*Nek2*$^{+/+}$ group. We conclude that inhibition of NEK2 reduces the accumulation of TAMs and Tregs.

NEK2 deficiency decreased the immunosuppressive activity of TAMs and MDSCs

To confirm our scRNA-seq findings, we quantified immune cell populations by flow cytometry from mouse BM and spleen (Figures 3A, 3B, S3A, and S3B). We observed a suppression of abnormal plasma cells (aPCs, CD19$^-$CD138$^+$), i.e., the injected 5TGM1 MM cells, in both the BM and spleen of 5TGM1/*Nek2*$^{-/-}$ compared with 5TGM1/*Nek2*$^{+/+}$ mice (Figure 3A). Decreases of Ly6C^{hi} macrophages (CD11b$^+$CD11c$^-$F4/80$^+$Ly6C^{hi}), Mo-MDSCs (CD11b$^+$CD11c$^-$F4/80$^-$Ly6C^{hi}Ly6G$^-$), and G-MDSCs (CD11b$^+$CD11c$^-$F4/80$^-$Ly6C^{int}Ly6G$^+$) were observed in the spleen of 5TGM1/*Nek2*$^{-/-}$ compared with 5TGM1/*Nek2*$^{+/+}$ mice (Figure 3A). However, these findings were not observed in the BM, because naive mouse BM may contain a significant number of normal myeloid cells that are phenotypically indistinguishable from MDSCs.[14] For the T cell populations, although no significant changes were observed in total T cells, an increase in the CD4/CD8 cell ratio was seen in the BM of 5TGM1/*Nek2*$^{+/+}$ compared with 5TGM1/*Nek2*$^{-/-}$ mice (Figure 3B). As expected, both CD4 and CD8 T cells had increased PD-1 expression in the 5TGM1/*Nek2*$^{+/+}$ compared with 5TGM1/*Nek2*$^{-/-}$ mice, suggesting that T cells were more inhibitory (Figure 3B). The percentages of either IFN-γ^+ or granzyme B$^+$ CD8 T cells showed

Figure 2. Loss of NEK2 reduces tumor-associated macrophages (TAMs) and Tregs

(A) Experimental layout.

(B) Serum IgG2b levels. n = 6–8 mice/group from two independent experiments with three technical replicates. Boxplot shows mean ± SD and the p value for the two-way ANOVA followed by Sidak multiple comparison test. $***p < 0.001$.

(C) Survival analysis. n = 10 mice/group. $**p < 0.01$

(D) Stacked bar charts representing of BM cell populations following 10X Genomics scRNA-seq workflow (n = 6,379 cells for *Nek2*$^{+/+}$, 5,746 cells for *Nek2*$^{-/-}$, 8,483 cells for 5TGM1/*Nek2*$^{+/+}$, and 9,676 cells for 5TGM1/*Nek2*$^{-/-}$ group).

(E) Violin plot representing NEK2 expression in immune cell populations identified in (D).

(F) Volcano plot showing differential gene expression in the macrophages of 5TGM1/*Nek2*$^{-/-}$ vs. 5TGM1/*Nek2*$^{+/+}$ group with a $|\log_2 FC| > 1$ and $p < 0.05$.

(G) KEGG analysis of downregulated genes in macrophages of 5TGM1/*Nek2*$^{-/-}$ vs. 5TGM1/*Nek2*$^{+/+}$ group.

(H) Representative reconstructed μCT images of tibia sagittal sections showing bone lytic lesions and trabecular architecture. n = 5–10 mice/group from two independent experiments.

(I) Quantitative histomorphometric analyses of TRAP-stained number of osteoclast surface per bone surface (Oc.S/BS) and osteoclast per bone perimeter (N.Oc/B.Pm). n = 10 mice/group from two independent experiments. n = 3 TRAP staining area from each slide were randomly selected and examined. Boxplot shows mean ± SD and the p value for two-tailed t test. $*p < 0.05$; $***p < 0.001$.

(J) KEGG analysis of upregulated genes in macrophages of 5TGM1/*Nek2*$^{-/-}$ vs. 5TGM1/*Nek2*$^{+/+}$ group.

(K) UMAP plots of macrophage subpopulations (left) and violin plots showing their marker genes (right).

(L) UMAP plots of NK/T subpopulations (left) and violin plots showing their marker genes (right). Please also see Figure S2 and Table S2.

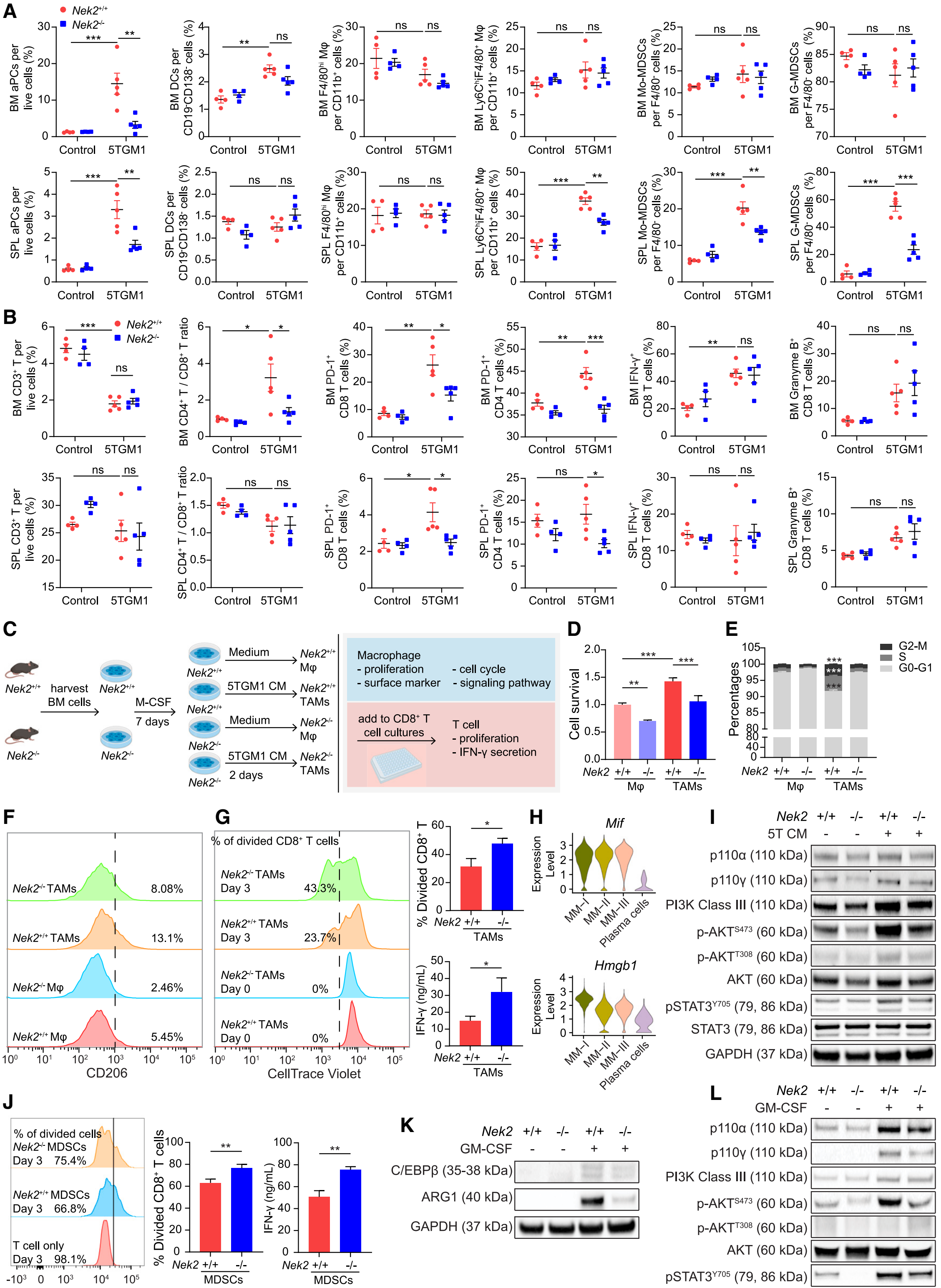

(legend on next page)

non-significant increases in the tumor-bearing groups compared with non-5TGM1 injected groups, but little or no differences between $Nek2^{+/+}$ and $Nek2^{-/-}$ (Figure 3B). These findings suggest that lack of NEK2 in the microenvironmental cells tends to inhibit the generation of functional TAMs and MDSCs as well as to decrease the inhibitory T cell populations.

Given that TAMs and MDSCs can be induced from naive BM cells via cytokines, we first tested the effect of NEK2 on the cytokine-induced generation of TAMs and MDSCs *in vitro* (Figure 3C). Macrophage colony stimulating factor (M-CSF) sufficiently induced macrophage maturation and adherence from both $Nek2^{+/+}$ and $Nek2^{-/-}$ mice (Figure S3C). 5TGM1 conditioned medium (CM) improved cell survival in $Nek2^{+/+}$ mice-derived macrophages, while $Nek2^{-/-}$ had lower macrophage survival (Figure 3D). NEK2 is known to regulate cell mitosis. We observed similar findings in the macrophage's cell cycle; i.e., 5TGM1 CM-treated $Nek2^{+/+}$ macrophages had higher S and G2/M populations compared with 5TGM1 CM-treated $Nek2^{-/-}$ macrophages (Figure 3E). 5TGM1 CM promoted CD206 expression compared with untreated macrophages, while NEK2 deficiency decreased CD206 (Figure 3F), suggesting that NEK2 promotes TAM differentiation. Moreover, TAMs induced from $Nek2^{-/-}$ mice promoted T cell proliferation and IFN-γ production compared to TAMs induced from $Nek2^{+/+}$ mice (Figure 3G). We hypothesize that NEK2 affects TAMs activation in response to tumor-secreted factors. scRNA-seq analysis of differentially expressed genes of 5TGM1 MM cells vs. plasma cells (Table S3) revealed *Mif* and *Hmgb1* were highly expressed in the MM cells (Figure 3H). To investigate whether NEK2 can promote the macrophage response to MIF-PI3K-AKT[30] and HMGB1-STAT3 signaling,[31] we performed western blots, which revealed that $Nek2^{+/+}$ TAMs had elevated levels of p110α, p110γ, PI3K class III, p-AKT (S473), and p-STAT3 (Y705) compared with unstimulated macrophages, while these levels were blocked in $Nek2^{-/-}$ TAMs (Figure 3I). Similar findings were observed in MDSCs between $Nek2^{+/+}$ and $Nek2^{-/-}$ mice (Figures 3J–3L), although no significant difference was observed in the percentages of G-MDSCs and Mo-MDSCs (Figure S3D). These findings suggest that NEK2 enhances the immunosuppressive function of TAMs and MDSCs.

MM patients with high expression of *NEK2* show an impaired T cell response

We investigated the patterns of *NEK2* gene expression in BM-derived, CD138-selected plasma cells from 324 MGUS, 303 SMM, 1049 NDMM, and 1066 RRMM from the University of Arkansas for Medical Sciences (UAMS) archive (UAMS-MM). *NEK2* mRNA level was increased in NDMM when compared with SMM and MGUS (Figure 4A) and further increased in RRMM relative to NDMM (Figure 4A). Moreover, *NEK2* was higher in HR MM compared with the low-risk (LR) MM as defined by the GEP70 score (Figure 4A). MM can be classified into seven molecular subtypes according to gene expression patterns,[32] where *NEK2* expression was highest in the proliferation (PR) subtype and lowest in the hyperdiploid (HY) subtype (Figure 4B). *NEK2* differences across MM subtypes were confirmed in the Multiple Myeloma Research Foundation's (MMRF) CoMMpass dataset, which includes 606 NDMM samples (Figure 4B). Kaplan-Meier analyses of UAMS-MM and MMRF CoMMpass data showed that MM patients with high expression of *NEK2* had inferior overall survival (OS) and progression-free survival (PFS) (Figures 4C and S4A).

To determine the correlation of *NEK2* expression levels with immune effector cells, we implemented mass cytometry (CyTOF) with an immune cell panel (Figure S4B). BM aspirate samples were divided into two groups, $NEK2^{high}$ (n = 6) and $NEK2^{low}$ (n = 6), based on *NEK2* expression in CD138-selected plasma cells. The $NEK2^{high}$ group had a higher average percentage of $CD38^{+}CD45^{-/dim}$ MM cells (Figure S4C), which were highly proliferative as indicated by an increase in average Ki67 stains (Figure S4D). tSNE plot of gated MM cells using equal events per sample indicated heterogeneity among patients (Figure S4E). To analyze immune cell subtypes and immune checkpoint expression, we conducted FlowSOM analysis on the gated

Figure 3. NEK2 deficiency decreased the immunosuppressive activity of TAMs and MDSCs

(A and B) Flow cytometric analysis showing the percentages of indicated cell populations in the BM and SPL of $Nek2^{+/+}$, $Nek2^{-/-}$, 5TGM1/$Nek2^{+/+}$, and 5TGM1/$Nek2^{-/-}$ mice. n = 4–5 mice/group from two independent experiments. Dot plot shows mean ± SD and the p value for the two-way ANOVA followed by Sidak multiple comparison test.

(C) Experimental layout. BM-derived macrophages were generated from $Nek2^{-/-}$ and $Nek2^{+/+}$ C57BL/KaLwRij mice after 7 days of M-CSF treatment. TAMs were induced by adding 5TGM1 conditioned medium (CM) for an additional 2 days followed by detection of macrophage survival, cell cycle, CD206 expression, and its effects on T cells proliferation and IFN-γ secretion.

(D) Prestoblue staining to detect mouse macrophage survival. n = 3 independent experiments, each with three technical replicates. Boxplot shows mean ± SD and the p value for the two-way ANOVA followed by Sidak multiple comparison test.

(E) Cell-cycle analyses of mouse macrophages. n = 3 independent experiments, each with three technical replicates. Boxplot shows mean ± SD and the p value for the two-way ANOVA followed by Sidak multiple comparison test.

(F) Flow cytometry analyses of CD206 expression on mouse macrophages. n = 3 independent experiments, each with three technical replicates.

(G) Representative histograms and quantification analysis showing the percentages of divided $CD8^{+}$ T cells co-cultured with TAMs on day 3 (left); IFN-γ levels in the co-culture supernatants on day 1 (right). n = 3 independent experiments, each with three technical replicates. Boxplot shows mean ± SD and the p value for two-tailed t test.

(H) Violin plot showing *Mif* and *Hmgb1* gene expression in MM and plasma cell populations identified in Figure 2D.

(I) Western blots analysis of cell lysates to detect PI3K and STAT3 pathway proteins in mouse TAMs and naive macrophages.

(J) Representative histograms and quantification analysis showing the percentages of divided $CD8^{+}$ T cells co-cultured with MDSCs on day 0 and day 3 (left); IFN-γ levels in the co-culture supernatants on day 1 (right). n = 3 independent experiments, each with three technical replicates. Boxplot shows mean ± SD and the p value for two-tailed t test.

(K and L) Western blots of cell lysates to detect C/EBPβ, arginase-1 (K), as well as PI3K and STAT3 pathway proteins (L) of MDSCs and freshly isolated $CD11b^{+}$ cells. ns, $p > 0.05$; *$p < 0.05$; **$p < 0.01$; ***$p < 0.001$. Please also see Figure S3 and Table S3.

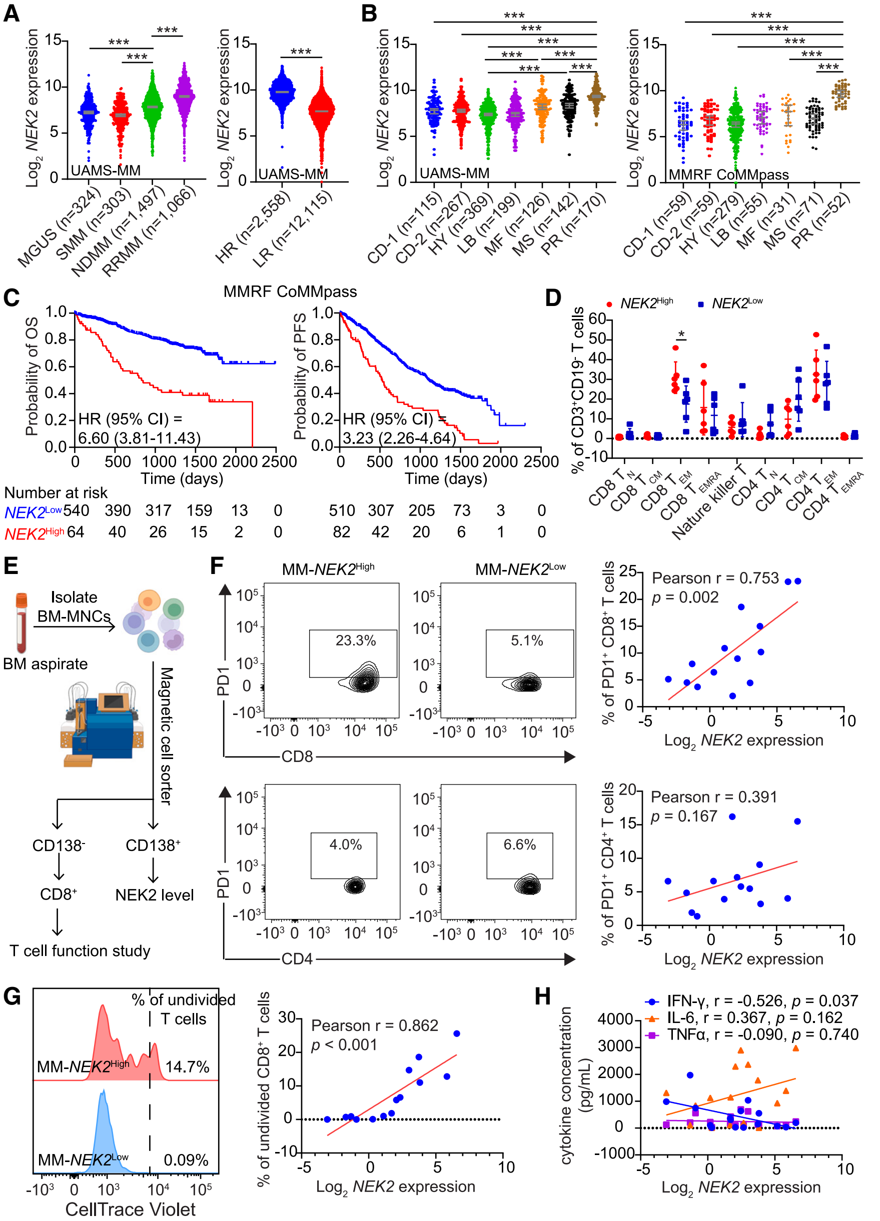

Figure 4. MM patients with high expression of *NEK2* show an impaired T cell response

(A) *NEK2* mRNA levels in UAMS-MM dataset among MGUS, SMM, NDMM, and RRMM (left), seven MM subtypes of NDMM (middle), and high risk (HR) vs. low risk (LR) (right). The seven MM subtypes include proliferation (PR), low bone disease (LB), MMSET (MS), hyperdiploid (HY), CCND1 (CD-1), CCND3 (CD-2), and MAF/MAFB (MF). *NEK2* expression was identified using probe 204641_at. Violin plot shows median ± 95% confidence interval and p value for one-way ANOVA followed by a Tukey's multiple comparison test.

(B) *NEK2* mRNA levels from 606 NDMM samples of MMRF CoMMpass dataset among seven MM subtypes. *NEK2* expression was identified with ENSG00000117650. Violin plot shows median ± 95% confidence interval and p value for one-way ANOVA followed by a Tukey's multiple comparison test.

(C) Kaplan-Meier analyses of overall survival (left) and progression-free survival (right) of NDMM patients from the MMRF CoMMpass dataset based on NEK2 expression. Median OS of *NEK2*^{high}: 2,207 days, *NEK2*^{Low}: undefined. Median PFS of *NEK2*^{high}: 804 days, *NEK2*^{Low}: 1,260 days.

(D) Mass cytometry analyses of T cell populations from primary human MM bone marrow mononuclear cells (BM-MNCs). n = 6/group. Dot plot shows mean ± SD and the p value for the two-way ANOVA followed by Sidak multiple comparison test.

(E) Experimental layout. Freshly isolated BM-MNCs of MM patients were processed to magnetic cell sorter to obtain paired CD138$^+$ MM cells and CD138$^-$ cells. CD138$^+$ MM cells were processed for RNA extraction to detect *NEK2* expression by qPCR. CD138$^-$ cells were enriched for CD8$^+$ T cells and cultured with Dynabeads Human T-Activator CD3/CD28 for T cell proliferation detection and cytokine detection of the culture supernatant.

(F) Flow cytometry analyses showing PD1 expression in CD8$^+$ and CD4$^+$ T cells from MM BM-MNCs (n = 14) and their correlation with *NEK2* mRNA expression levels of MM cells. Red line represents simple linear regression. Pearson correlation coefficient (r) was noted in the figure.

(G) Proliferation analyses of human CD8$^+$ T cells (n = 14) after stimulation with Dynabeads Human T-Activator CD3/CD28 for 5 days (left). Correlation analysis of percentages of undivided CD8$^+$ T cells with *NEK2* mRNA expression levels of MM cells (right).

(H) Correlation analyses of *NEK2* mRNA expression levels of MM cells with IFN-γ, IL6, and TNFα concentrations in the culture supernatant of CD8$^+$ cells after stimulation with Dynabeads Human T-Activator CD3/CD28 for 24 h (n = 16). *p < 0.05; ***p < 0.0001. Please also see Figure S4.

CD45$^+$ cells. FlowSOM identified 10 major cell types based on their phenotype markers as indicated in the heatmap (Figures S4F–S4G). There was a modest decrease in CD8$^+$ T cell populations in the *NEK2*^{low} group that was not statistically significant (Figure S4H) probably due to the limited number of samples and high tumor heterogeneity. Because T cells are the most abundant cell population in MM patients and have been reported to correlate with patient outcomes,[33] we further analyze the subclusters of T cells and T cell activation status. The results showed that most T cells were in an end stage activation status. Specifically, T_{EM} and T_{EMRA} cells were most abundant among CD8$^+$ T cells, while T_{EM} and T_{CM} (T central memory) cells were most abundant among CD4$^+$ T cells; T_N were least represented in both CD4$^+$ and CD8$^+$ T cells (Figure 4D). A decrease of CD8$^+$ T_{EM} cells was found in *NEK2*^{low} group (Figure 4D). In addition, the percentage of PD1$^+$ CD8$^+$ T cells was significantly correlated with *NEK2* expression (Figures 4E and 4F). A reduced CD8$^+$ T cell proliferative capacity was observed in MM samples with high *NEK2* expression (Figure 4G). Also, the production of IFN-γ by CD8$^+$ T cells was negatively correlated with NEK2 expression levels, but no change was observed for TNFα and IL-6 (Figure 4H). These results indicate that *NEK2* is a prognostic marker for MM, and high *NEK2* in tumor cells is associated with an impaired T cell function.

NEK2 suppresses the IFN-γ/PD-L1 signaling pathway in MM patients

We observed an inverse correlation between an IFN-γ gene signature and a CIN gene signature (Figure 5A). Consistent with our animal studies (Figure 1G), we also observed that the IFN-γ-inducing gene CD274 was negatively correlated with *NEK2* expression in the NDMM samples in both the UAMS-MM and MMRF CoMMpass datasets (Figure 5B). CD274 showed the highest expression in the HY subtype and the lowest in the PR subtype (Figure 5C), which is in line with other studies showing PD-L1 is increased in hyperdiploid patients based on flow cytometry data.[34] To determine whether combining the expression of *NEK2* and *CD274* better predicts patient outcomes, we divided patients into four groups, $NEK2^{high}CD274^{high}$, $NEK2^{high}CD274^{low}$, $NEK2^{low}CD274^{high}$, and $NEK2^{low}CD274^{low}$. Kaplan-Meier analysis showed patients with $NEK2^{low}CD274^{high}$ had the best OS and PFS (Figure 5D). To validate the correlation of NEK2 and PD-L1 expression at the protein level, we conducted immunohistochemistry (IHC) analysis of NEK2 and PD-L1 on 50 BM biopsy of NDMM samples. Plotting the percentage of PD-L1-positive vs. NEK2-positive cells revealed that protein levels of NEK2 and PD-L1 were negatively correlated (Figure 5E). These results suggested that the IFN-γ/PD-L1 signaling axis is suppressed in MM cells with high NEK2.

Combining NEK2 inhibition with anti-PD-L1 mAb therapy provides therapeutic benefits

Based on the finding that NEK2 inhibition impaired TAMs and MDSCs function, while upregulating PD-L1 expression in MM cells, we hypothesized that combination of a NEK2 inhibitor, INH154, with anti-PD-L1 mAb would have additional therapeutic benefits. To test the hypothesis, we treated BM-MNCs *in vitro* (Figure 6A). INH154 treatment significantly decreased the percentages of $CD138^+$ MM cells (Figure 6B), suggesting INH154 selectively targeted MM cells probably due to their relatively high proliferative capacity. No significant killing effects were observed with the PD-L1 mAb on MM cells, which may be due to the limited function of antibody-dependent cell-mediated cytotoxicity. The increase in PD-L1 expression on MM cells and myeloid cells after INH154 treatment was effectively blocked by PD-L1 mAb treatment (Figures 6C and 6D). In addition, total T cells were increased after INH154 and the combination treatment, while $CD8^+$ and $CD4^+$ T cell percentages among total T cells were not significantly changed (Figure 6E). Moreover, the percentages of $PD1^+$ $CD8^+$ and $CD4^+$ T cells both decreased after INH154 and in the combination treatment (Figure 6F). These data indicate that NEK2 blockade selectively inhibited MM cell growth and reduced $PD1^+$ T cells in primary myeloma samples and combined with PD-L1 mAb provides better therapeutic benefits by blocking PD-L1 expression on MM and monocytes, which was increased after NEK2 inhibition.

To test the efficacy of the combination therapy on a well-established preclinical Vκ*MYC MM mouse model, INH154 and PD-L1 mAb were given alone or in combination 1 day prior to Vκ12653 MM cell injection and followed by administration twice a week for 5 weeks (Figure 7A). Both IHN154 and PD-L1 mAb decreased serum γ-globulin levels on day 35 post Vκ12653 MM cell injection when treated alone, and a further decrease was observed with combination treatment (Figures 7B and S5A). In addition, Kaplan-Meier survival analysis revealed a significant prolongation in survival in the combination-treatment group (Figure 7C). The weight of the spleen was lower in both INH154 and PD-L1 mAb-treated mice and further lowered by combination treatment (Figures 7D and S5B). Flow cytometry analysis of $CD138^+B220^-$ MM cell percentage and its PD-L1 expression level in the BM and spleen showed dramatic decreases of MM cell percentages in the combination-treated group (Figures 7E, 7F, and S5C). In addition, PD-L1 expression on the MM cells slightly increased after INH154 treatment while being almost completely blocked after PD-L1 mAb treatment (Figures 7E, 7F, and S5C). These data demonstrate that NEK2 inhibitor INH154 significantly enhanced the antitumor efficacy of the anti-PD-L1 mAb by increasing the PD-L1 level and enhancing $CD8^+$ T cell activity.

DISCUSSION

Our study strongly suggests that blocking of NEK2 in the environment delays MM tumor progression by augmenting antitumor immunity. Specifically, NEK2 deficiency in myeloid progenitor cells decreased the generation of functional TAMs and MDSCs, which in turn enhanced the antitumor function of T cells. By assessing the clinical significance of NEK2 in MM immunity, we found that higher NEK2 expression is associated with an increased frequency of $CD8^+$ T_{EM} cells, and a lower level of NEK2 enriches for an IFN-γ gene signature associated with an elevated expression of PD-L1. The NEK2 inhibitor INH154 significantly enhanced the antitumor efficacy of the anti-PD-L1 mAb by increasing the PD-L1 level and enhancing $CD8^+$ T cell activity.

Previous studies have reported that peripheral blood levels of IFN-γ are decreased in MM patients compared with healthy controls.[35] Multi-site cohort analysis of gene expression datasets of plasma cells reveals that an enhanced immune gene signature correlates with MM patient's outcome with higher levels of IFN-γ and other Th1 cytokines predicting longer survival.[36] However, how the immune gene signature is altered in tumor cells lacks experimental evidence. In this study, we incorporated comprehensive experimental tools to study how NEK2 expression affects MM immunity. Our data identified the association of high NEK2 expression with adverse outcomes and a downregulated IFN-γ gene signature, resulting in an elevated infiltration of $PD1^+$ $CD8^+$ T_{EM} cells, suggesting that the activation of IFN-γ gene signature in MM cells may be generated by the activation of $CD8^+$ T cell responses. The PD-L1 expression in the MM cells likely serves as a surrogate marker for IFN-γ signaling and is an indicator of antitumor Th1 response, but whether it plays a role in tumor anti-apoptosis and immune escape needs further investigation. In addition, we identified that NEK2 knockout significantly decreased TAMs and Tregs in the 5TGM1 MM mouse model. This is consistent with recent clinical scRNA-seq studies showing that an immune suppressive BM microenvironment contains increased percentages of exhausted T cells and myeloid cells during MM progression and relapse.[13,37] Thus, modulating MM immune microenvironmental cells and restoring $CD8^+$ T cell immunity[11,38] may be an attractive strategy to prevent MM tumor growth. Notably, NEK2 knockout does not

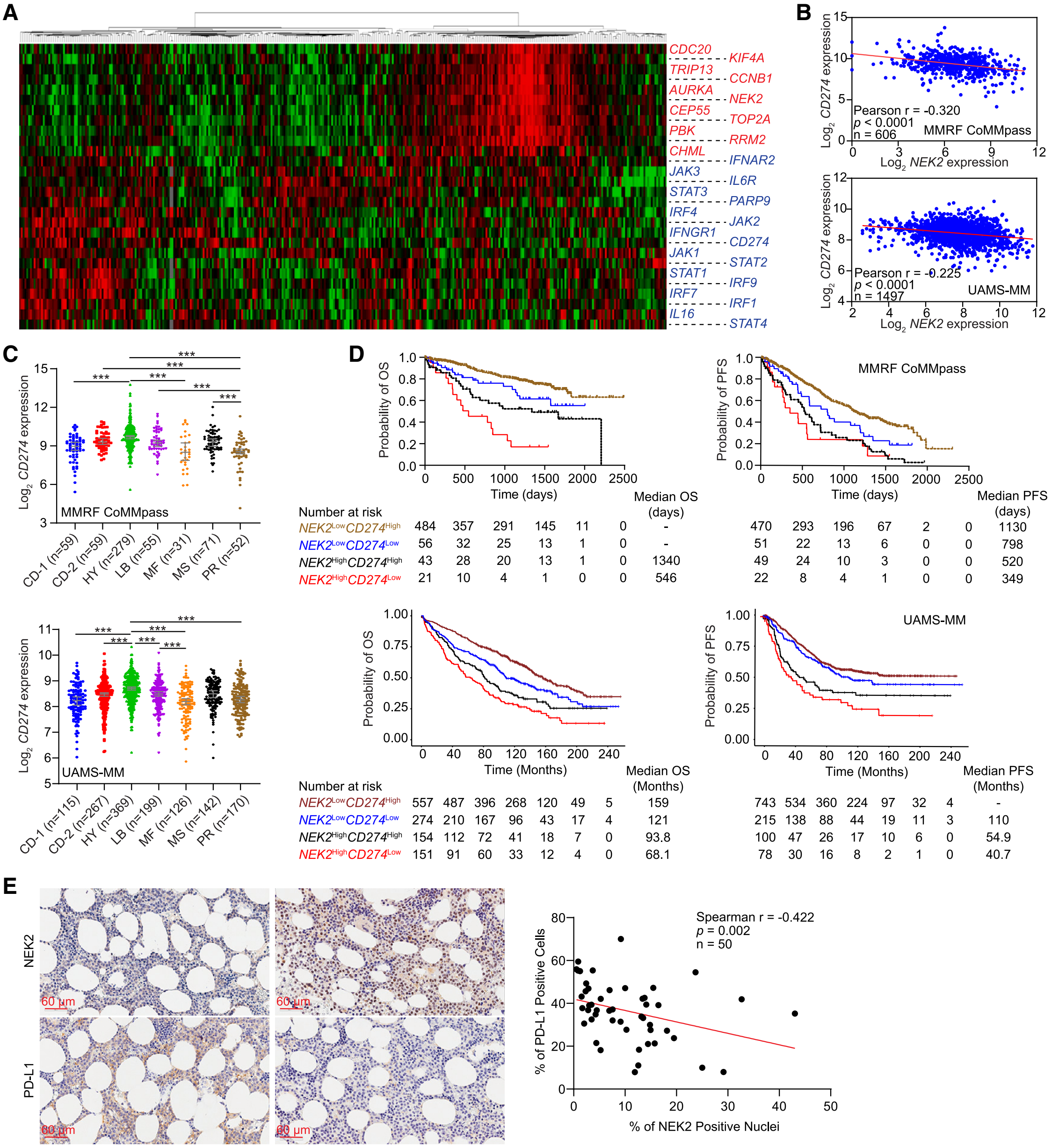

Figure 5. NEK2 suppresses the IFN-γ/PD-L1 signaling pathway in MM patients

(A) Heatmap of CIN and IFN-γ signaling genes from NDMM patients in the TT2 cohort (n = 351).

(B) Correlation analyses of *CD274* and *NEK2* mRNA from NDMM samples derived from MMRF CoMMpass (n = 606) and UAMS-MM (n = 1,497) datasets. *CD274* expression was identified using probe 223834_at in UAMS-MM and ENSG00000120217 in the MMRF CoMMpass dataset. Red line represents simple linear regression. Pearson correlation coefficient (r) was noted in the figure.

(C) Dot plots of *CD274* mRNA expression among seven MM subtypes of NDMM samples from MMRF CoMMpass (n = 606) and UAMS-MM (n = 1,388 that are subtypes available) datasets. Violin plot shows median ± 95% confidence interval and p value for one-way ANOVA followed by a Tukey's multiple comparison test.

(D) Kaplan-Meier analyses of overall survival (left) and progression-free survival (right) from NDMM patients of MMRF CoMMpass and UAMS-MM datasets based on *NEK2* and *CD274* expression.

(E) IHC staining of NEK2 and PD-L1 expression on 50 bone marrow biopsies derived from NDMM patients (40×, scale bar represents 60 μm). Correlation analysis of percentages of NEK2-positive nuclei and PD-L1-positive cells. Red line represents simple linear regression. Spearman correlation coefficient (r) was noted in the figure. ***$p < 0.0001$.

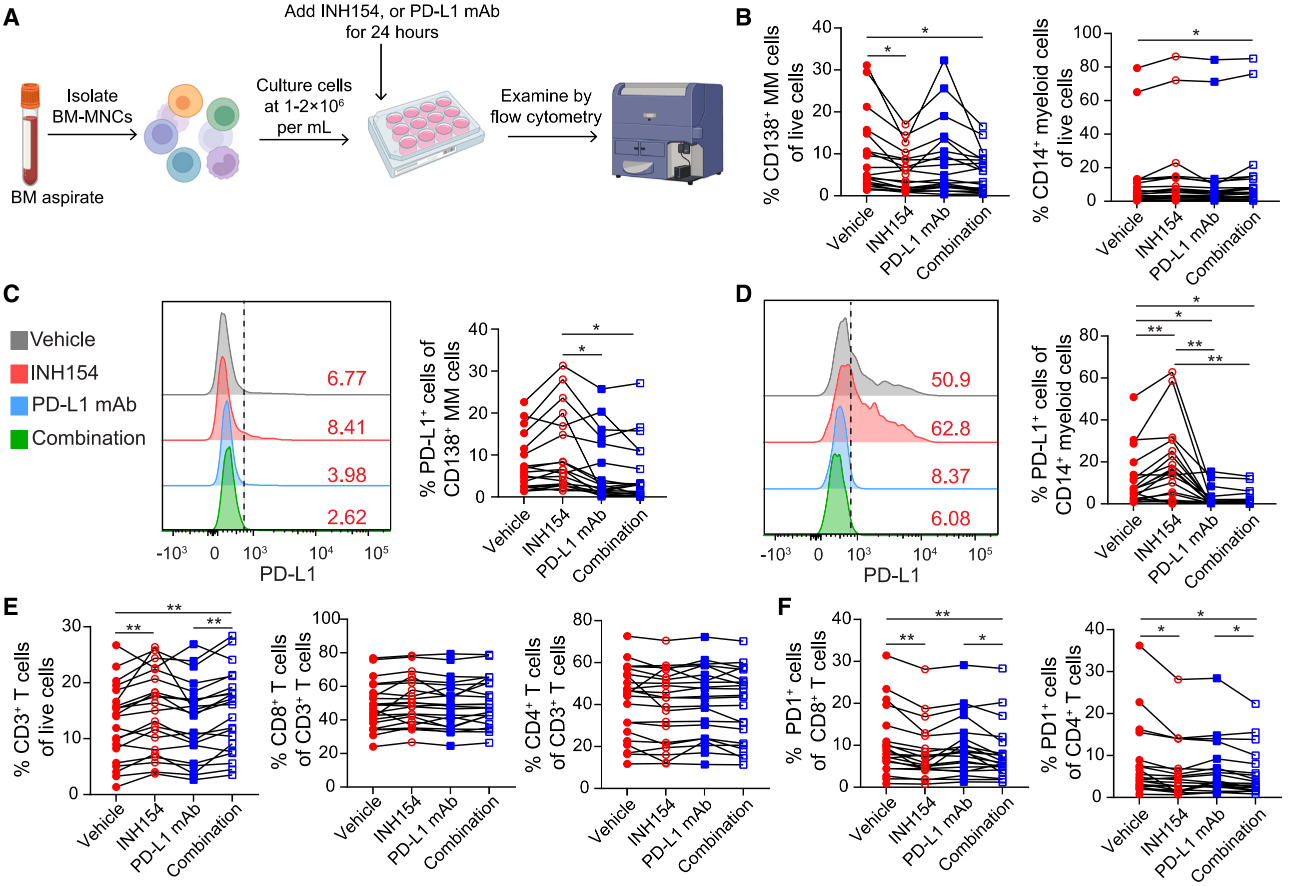

Figure 6. NEK2 inhibition increases potency of anti-PD-L1 monoclonal antibody (mAb) against MM

(A) Experimental layout for a combination treatment of INH154 and PD-L1 mAb in freshly isolated BM-MNCs *in vitro*. Survived CD138$^+$ MM cells, CD14$^+$ myeloid cells, CD8$^+$ T cells, and CD4$^+$ T cells and their PD-L1 or PD1 expression were detected 24 h after the treatment by flow cytometry.

(B) Flow cytometry analysis showing percentages of CD138$^+$ MM cells and CD14$^+$ monocytes of total live cells after treatments.

(C and D) Flow cytometry analysis showing PD-L1 expression in CD138$^+$ MM cells (C) and CD14$^+$ monocytes (D) after treatments.

(E) Flow cytometry analysis showing percentages of CD3$^+$ of total live cells and CD8$^+$ and CD4$^+$ T cells of total CD3$^+$ T cells after treatments.

(F) Flow cytometry analysis showing PD1 expression in CD8$^+$ T cells and CD4$^+$ T cells after treatments. (B–F) Spaghetti plots show data from each patient and p value for randomized block (repeated measures) ANOVA followed by a Tukey's multiple comparison test. *$p < 0.05$; **$p < 0.01$; ***$p < 0.001$.

modulate naive macrophages, indicating NEK2 facilitates macrophage response to the soluble factor secreted by the tumor cells. In a different light, high NEK2 expression in tumor cells may result in increased secretion of the immune regulating soluble factors that are worth further investigation.

The level of PD-L1 expression in HR and relapsed MM cells is relatively low, which may explain why responses to PD-L1/PD1 blockade monotherapy in MM have been limited.[39,40] This is especially true given that basal expression of PD-L1 on tumor cells can predict the sensitivity of pembrolizumab.[41] Combining PD-L1/PD1 blockades with immunomodulators has shown a potential synergy.[42,43] However, increased serious adverse events and decreased OS were seen.[44–46] Therefore, more efficient and safer combination strategies are needed. In this study, we found that NEK2 inhibition increased IFN-γ signaling and PD-L1 expression in MM cells in both animal models and clinical datasets. In support of that, studies have shown that PD-L1 expression in MM cells is increased in the presence of IFN-γ,[47,48] while changes in tumor antigen presentation and IFN-γ signaling pathways play an essential role in primary and acquired resistance of PD-L1/PD-1 blockade.[49,50] We observed that PD-L1 expression was highest in the HY subtype and lowest in the PR subtype of MM, suggesting that increasing IFN-γ$^+$ CD8$^+$ T cells tumor surveillance may protect HY subgroup MM from progression to PR. MM patients in the HY subtype may therefore be relatively sensitive to the PD-L1/PD-1 blockade. Furthermore, our findings showed a significant augmentation of antitumor activity of an anti-PD-L1 mAb by a NEK2 inhibitor in primary MM samples cultured *in vitro* as well as in an MM mouse model. We provided initial experimental evidence that further clinical investigation of a NEK2 inhibitor in combination with PD-L1 blockade may be warranted. Notably, overexpression of PD-L1 exhibits anti-apoptotic tumor characteristics acting as a shield for tumor cells to protect tumor cells from T cell-mediated elimination.[51] Thus, upregulating tumor PD-L1 levels inhibits T cell-mediated cytotoxicity, and

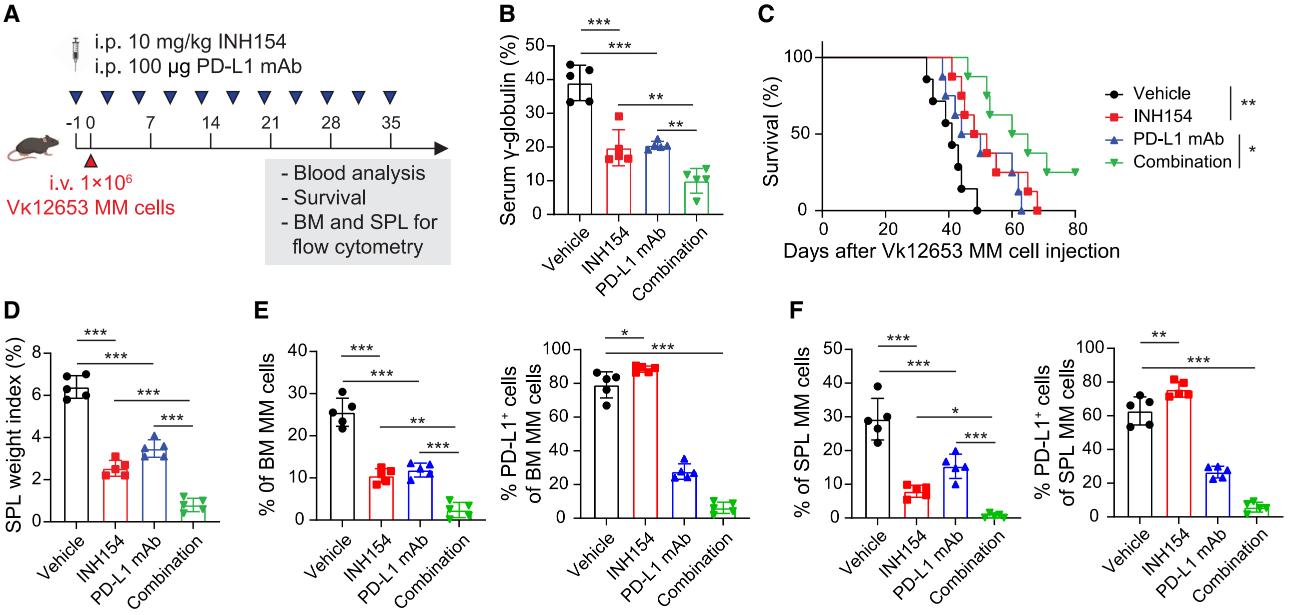

Figure 7. Combining NEK2 inhibition with anti-PD-L1 mAb therapy provides therapeutic benefits in MM mouse model

(A) Experimental timeline for a combination treatment of INH154 and PD-L1 mAb in C57BL/6 mice injected with Vκ12653 MM cells. MM was monitored by serum protein electrophoresis to detect γ-globulin. Survival was monitored up to 80 days post Vκ12653 MM cells injection. Endpoint of MM engraftment was analyzed BM and SPL by fluorescence-activated cell sorting on day 35 post Vκ12653 MM cell injection when mice in the control group were moribund.

(B) Quantitative analyses of mouse serum γ-globulin percentages on day 35 post Vκ12653 MM cell injection. n = 5 mice/group with two biological replicates. Boxplot shows mean ± SD and p value for one-way ANOVA followed by a Tukey's multiple comparison test.

(C) Survival analysis.

(D) SPL weight index. n = 5 mice/group with two biological replicates. Boxplot shows mean ± SD and p value for one-way ANOVA followed by a Tukey's multiple comparison test.

(E and F) Flow cytometry analysis showing percentages of CD138$^+$B220$^-$ MM cells and PD-L1 expression in MM cells in BM (E) and SPL (F). n = 5 mice/group with two biological replicates. Boxplot shows mean ± SD and p value for one-way ANOVA followed by a Tukey's multiple comparison test. *$p < 0.05$; **$p < 0.01$; ***$p < 0.001$. Please also see Figure S5.

compounds that can downregulate PD-L1 should achieve better antitumor effects.[52] It's worth noting that our observation regarding the role of NEK2 in PD-L1 regulation is inconsistent with a pancreatic cancer study showing that NEK2 phosphorylates PD-L1 to stabilize its expression.[25] The interplay between NEK2 and PD-L1 regulation may be context dependent, influenced by tumor-specific characteristics and the specific immune microenvironment within each cancer type. Further investigation is needed to unravel the underlying mechanisms governing NEK2-PD-L1 interactions in diverse cancer types.

Limitations of the study

The *Nek2*$^{-/-}$ mouse used in this study is a whole-body knockout mouse model. Additional experiments using conditional knockout of NEK2 only in myeloid cells would be important to prove the conclusion that NEK2 deficiency in myeloid cells suppresses differentiation of TAMs and MDSCs and enhances the antitumor function of T cells in the MM mouse model.

STAR★METHODS

Detailed methods are provided in the online version of this paper and include the following:

- KEY RESOURCES TABLE
- RESOURCE AVAILABILITY
  - ○ Lead contact
  - ○ Materials availability
  - ○ Data and code availability
- EXPERIMENTAL MODEL AND STUDY PARTICIPANT DETAILS
  - ○ Mice
  - ○ Generation of *Nek2* knockout mice
  - ○ Pre-tumoral analysis of Eμ-myc model
  - ○ Transplantable multiple myeloma mouse models
- METHOD DETAILS
  - ○ *In vivo* treatment
  - ○ Mouse serum protein electrophoresis
  - ○ Flow cytometry
  - ○ Bulk RNA sequence
  - ○ Single cell RNA sequence (scRNA-seq)
  - ○ Bioinformatics analysis
  - ○ Micro-computed tomography (μCT)
  - ○ Bone histomorphometry
  - ○ *In vitro* TAMs and MDSCs generation
  - ○ Functional Assay of T Cells Co-cultured with TAMs or MDSCs
  - ○ Cell viability and cell cycle

  - ○ Western Blot
  - ○ Isolation and Purification of human myeloma cells
  - ○ Gene expression profiling
  - ○ Quantitative real-time PCR (qRT-PCR)
  - ○ Functional Assays of human T cells
  - ○ Immunohistochemistry (IHC)
  - ○ Mass cytometry (CyTOF)
  - ○ *In vitro* treatment of primary BM-MNCs
- QUANTIFICATION AND STATISTICAL ANALYSIS

SUPPLEMENTAL INFORMATION

Supplemental information can be found online at https://doi.org/10.1016/j.xcrm.2023.101214.

ACKNOWLEDGMENTS

We thank all the patients who supported our study. We thank the Multiple Myeloma Research Foundation (MMRF) for providing the CoMMpass dataset (https://research.themmrf.org and www.themmrf.org). We thank Bipharm Inc. for providing NEK2 inhibitor INH154. We thank the Genomics Division of the Iowa Institute of Human Genetics and the University of Iowa Carver College of Medicine for RNA-seq study. We thank Sarah K. Johnson at University of Arkansas for Medical Sciences (UAMS), Jessica Watson at Standard BioTools (formerly Fluidigm), and Qianjun Zhang at Cytobank for the mass cytometry study. Great thanks is given to the UAMS Core facilities—Tissue Biorepository and Procurement Core, Genomics Core Laboratory, Experimental Pathology Core, Flow Cytometry Core Facility, Digital Microscopy Core Laboratory, Bone Core, and Arkansas Children's Hospital—for their help. This work was supported by National Cancer Institute 1R01CA236814-01A1 (F.Z.), 3R01-CA236814-03S1 (F.Z.), R01 CA151354 (S.J.), R01 CA234181 (M.C.), U54CA272691-01 (F.Z. and J.D.S.), US Department of Defense (DoD) CA180190 (F.Z.), Translational Research Institute Pilot Award KL2 TR003108 (C.A.), Myeloma Crowd Research Initiative Award (F.Z.), Paula and Rodger Riney Foundation (F.Z.), and UAMS Winthrop P. Rockefeller Cancer Institute (WRCRI) Fund (F.Z.). Illustrations were created using Biorender software.

AUTHOR CONTRIBUTIONS

Conceptualization, Y.C., F.S., and F.Z.; methodology, Y.C., F.S., D.V.A., J.-R.C., M.C., and P.L.B.; software, Y.C., F.S., V.W., W.G., D.M., C.A., M.A.B., and I.N.; data curation, Y.C., F.S., V.W., W.G., D.M., M.A.B., and I.N.; formal analysis, Y.C., F.S., D.V.A., E.R.S., J.Y., and F.Z.; investigation, Y.C., F.S., H.C., Y.Z., D.G., B.P., H.X., and F.Z.; resources, C.B., J.D.S., M.C., P.L.B., and F.Z.; supervision, G.T., J.D.S., and F.Z.; visualization, Y.C. and F.S.; writing – original draft, Y.C. and F.S.; writing – review & editing, all authors; funding acquisition, C.A., M.C., S.J., and F.Z.

DECLARATION OF INTERESTS

The authors declare that they have filed for patents related to this work. M.C. and P.L.B have rights to Vκ*MYC technology licensing. S.A.H reports receiving honorarium from Jansen and Sanofi.

INCLUSION AND DIVERSITY

We support inclusive, diverse, and equitable conduct of research.

Received: April 17, 2023
Revised: July 21, 2023
Accepted: September 8, 2023
Published: October 3, 2023

REFERENCES

1. Rajkumar, S.V. (2022). Multiple myeloma: 2022 update on diagnosis, risk stratification, and management. Am. J. Hematol. *97*, 1086–1107. https://doi.org/10.1002/ajh.26590.
2. Alyea, E., Weller, E., Schlossman, R., Canning, C., Webb, I., Doss, D., Mauch, P., Marcus, K., Fisher, D., Freeman, A., et al. (2001). T-cell–depleted allogeneic bone marrow transplantation followed by donor lymphocyte infusion in patients with multiple myeloma: induction of graft-versus-myeloma effect. Blood *98*, 934–939. https://doi.org/10.1182/blood.v98.4.934.
3. Lokhorst, H.M., Schattenberg, A., Cornelissen, J.J., Thomas, L.L., and Verdonck, L.F. (1997). Donor leukocyte infusions are effective in relapsed multiple myeloma after allogeneic bone marrow transplantation. Blood *90*, 4206–4211.
4. Tricot, G., Vesole, D.H., Jagannath, S., Hilton, J., Munshi, N., and Barlogie, B. (1996). Graft-versus-myeloma effect: proof of principle. Blood *87*, 1196–1198.
5. Ri, M., Suzuki, K., Ishida, T., Kuroda, J., Tsukamoto, T., Teshima, T., Goto, H., Jackson, C.C., Sun, H., Pacaud, L., et al. (2022). Ciltacabtagene autoleucel in patients with relapsed/refractory multiple myeloma: CARTITUDE-1 (phase 2) Japanese cohort. Cancer Sci. *113*, 4267–4276. https://doi.org/10.1111/cas.15556.
6. Martin, T., Lin, Y., Agha, M., Cohen, A.D., Htut, M., Stewart, A.K., Hari, P., Berdeja, J.G., Usmani, S.Z., Yeh, T.M., et al. (2022). Health-related quality of life in patients given ciltacabtagene autoleucel for relapsed or refractory multiple myeloma (CARTITUDE-1): a phase 1b-2, open-label study. Lancet. Haematol. *9*, e897–e905. https://doi.org/10.1016/S2352-3026(22)00284-8.
7. Zhao, W.H., Wang, B.Y., Chen, L.J., Fu, W.J., Xu, J., Liu, J., Jin, S.W., Chen, Y.X., Cao, X.M., Yang, Y., et al. (2022). Four-year follow-up of LCAR-B38M in relapsed or refractory multiple myeloma: a phase 1, single-arm, open-label, multicenter study in China (LEGEND-2). J. Hematol. Oncol. *15*, 86. https://doi.org/10.1186/s13045-022-01301-8.
8. Cohen, A.D., Hari, P., Htut, M., Berdeja, J.G., Usmani, S.Z., Madduri, D., Olyslager, Y., Goldberg, J.D., Schecter, J.M., Jackson, C.C., et al. (2023). Patient Perceptions Regarding Ciltacabtagene Autoleucel Treatment: Qualitative Evidence From Interviews With Patients With Relapsed/Refractory Multiple Myeloma in the CARTITUDE-1 Study. Clin. Lymphoma, Myeloma & Leukemia *23*, 68–77. https://doi.org/10.1016/j.clml.2022.10.001.
9. Zelle-Rieser, C., Thangavadivel, S., Biedermann, R., Brunner, A., Stoitzner, P., Willenbacher, E., Greil, R., and Jöhrer, K. (2016). T cells in multiple myeloma display features of exhaustion and senescence at the tumor site. J. Hematol. Oncol. *9*, 116. https://doi.org/10.1186/s13045-016-0345-3.
10. Dhodapkar, K.M., Cohen, A.D., Kaushal, A., Garfall, A.L., Manalo, R.J., Carr, A.R., McCachren, S.S., Stadtmauer, E.A., Lacey, S.F., Melenhorst, J.J., et al. (2022). Changes in Bone Marrow Tumor and Immune Cells Correlate with Durability of Remissions Following BCMA CAR T Therapy in Myeloma. Blood Cancer Discov. *3*, 490–501. https://doi.org/10.1158/2643-3230.BCD-22-0018.
11. Guillerey, C., Harjunpää, H., Carrié, N., Kassem, S., Teo, T., Miles, K., Krumeich, S., Weulersse, M., Cuisinier, M., Stannard, K., et al. (2018). TIGIT immune checkpoint blockade restores CD8(+) T-cell immunity against multiple myeloma. Blood *132*, 1689–1694. https://doi.org/10.1182/blood-2018-01-825265.
12. Speiser, D.E., Utzschneider, D.T., Oberle, S.G., Münz, C., Romero, P., and Zehn, D. (2014). T cell differentiation in chronic infection and cancer: functional adaptation or exhaustion? Nat. Rev. Immunol. *14*, 768–774. https://doi.org/10.1038/nri3740.
13. Tirier, S.M., Mallm, J.P., Steiger, S., Poos, A.M., Awwad, M.H.S., Giesen, N., Casiraghi, N., Susak, H., Bauer, K., Baumann, A., et al. (2021). Subclone-specific microenvironmental impact and drug response in refractory

multiple myeloma revealed by single-cell transcriptomics. Nat. Commun. *12*, 6960. https://doi.org/10.1038/s41467-021-26951-z.

14. Nakamura, K., Kassem, S., Cleynen, A., Chrétien, M.L., Guillerey, C., Putz, E.M., Bald, T., Förster, I., Vuckovic, S., Hill, G.R., et al. (2018). Dysregulated IL-18 Is a Key Driver of Immunosuppression and a Possible Therapeutic Target in the Multiple Myeloma Microenvironment. Cancer Cell *33*, 634–648.e5. https://doi.org/10.1016/j.ccell.2018.02.007.
15. Hofbauer, D., Mougiakakos, D., Broggini, L., Zaiss, M., Büttner-Herold, M., Bach, C., Spriewald, B., Neumann, F., Bisht, S., Nolting, J., et al. (2021). beta(2)-microglobulin triggers NLRP3 inflammasome activation in tumor-associated macrophages to promote multiple myeloma progression. Immunity *54*, 1772–1787.e9. https://doi.org/10.1016/j.immuni.2021.07.002.
16. Sun, J., Park, C., Guenthner, N., Gurley, S., Zhang, L., Lubben, B., Adebayo, O., Bash, H., Chen, Y., Maksimos, M., et al. (2022). Tumor-associated macrophages in multiple myeloma: advances in biology and therapy. J. Immunother. Cancer *10*, e003975. https://doi.org/10.1136/jitc-2021-003975.
17. Zhang, D., Huang, J., Wang, F., Ding, H., Cui, Y., Yang, Y., Xu, J., Luo, H., Gao, Y., Pan, L., et al. (2021). BMI1 regulates multiple myeloma-associated macrophage's pro-myeloma functions. Cell Death Dis. *12*, 495. https://doi.org/10.1038/s41419-021-03748-y.
18. Su, X., Xu, Y., Fox, G.C., Xiang, J., Kwakwa, K.A., Davis, J.L., Belle, J.I., Lee, W.C., Wong, W.H., Fontana, F., et al. (2021). Breast cancer-derived GM-CSF regulates arginase 1 in myeloid cells to promote an immunosuppressive microenvironment. J. Clin. Invest. *131*, e145296. https://doi.org/10.1172/JCI145296.
19. Yofe, I., Landsberger, T., Yalin, A., Solomon, I., Costoya, C., Demane, D.F., Shah, M., David, E., Borenstein, C., Barboy, O., et al. (2022). Anti-CTLA-4 antibodies drive myeloid activation and reprogram the tumor microenvironment through FcgammaR engagement and type I interferon signaling. Nat. Can. (Ott.) *3*, 1336–1350. https://doi.org/10.1038/s43018-022-00447-1.
20. Minnie, S.A., Waltner, O.G., Ensbey, K.S., Olver, S.D., Collinge, A.D., Sester, D.P., Schmidt, C.R., Legg, S.R., Takahashi, S., Nemychenkov, N.S., et al. (2023). TIGIT inhibition and lenalidomide synergistically promote anti-myeloma immune responses after stem cell transplantation in mice. J. Clin. Invest. *133*, e157907. https://doi.org/10.1172/JCI157907.
21. Zhou, W., Yang, Y., Xia, J., Wang, H., Salama, M.E., Xiong, W., Xu, H., Shetty, S., Chen, T., Zeng, Z., et al. (2013). NEK2 induces drug resistance mainly through activation of efflux drug pumps and is associated with poor prognosis in myeloma and other cancers. Cancer Cell *23*, 48–62. https://doi.org/10.1016/j.ccr.2012.12.001.
22. Franqui-Machin, R., Hao, M., Bai, H., Gu, Z., Zhan, X., Habelhah, H., Jethava, Y., Qiu, L., Frech, I., Tricot, G., and Zhan, F. (2018). Destabilizing NEK2 overcomes resistance to proteasome inhibition in multiple myeloma. J. Clin. Invest. *128*, 2877–2893. https://doi.org/10.1172/JCI98765.
23. Peres de Oliveira, A., Kazuo Issayama, L., Betim Pavan, I.C., Riback Silva, F., Diniz Melo-Hanchuk, T., Moreira Simabuco, F., and Kobarg, J. (2020). Checking NEKs: Overcoming a Bottleneck in Human Diseases. Molecules *25*, 1778. https://doi.org/10.3390/molecules25081778.
24. Gu, Z., Zhou, W., Huang, J., Yang, Y., Wendlandt, E., Xu, H., He, X., Tricot, G., and Zhan, F. (2014). Nek2 is a novel regulator of B cell development and immunological response. BioMed Res. Int. *2014*, 621082. https://doi.org/10.1155/2014/621082.
25. Zhang, X., Huang, X., Xu, J., Li, E., Lao, M., Tang, T., Zhang, G., Guo, C., Zhang, X., Chen, W., et al. (2021). NEK2 inhibition triggers anti-pancreatic cancer immunity by targeting PD-L1. Nat. Commun. *12*, 4536. https://doi.org/10.1038/s41467-021-24769-3.
26. Dana, D., Das, T., Choi, A., Bhuiyan, A.I., Das, T.K., Talele, T.T., and Pathak, S.K. (2022). Nek2 Kinase Signaling in Malaria, Bone, Immune and Kidney Disorders to Metastatic Cancers and Drug Resistance: Progress on Nek2 Inhibitor Development. Molecules *27*. https://doi.org/10.3390/molecules27020347.
27. House, I.G., Savas, P., Lai, J., Chen, A.X.Y., Oliver, A.J., Teo, Z.L., Todd, K.L., Henderson, M.A., Giuffrida, L., Petley, E.V., et al. (2020). Macrophage-Derived CXCL9 and CXCL10 Are Required for Antitumor Immune Responses Following Immune Checkpoint Blockade. Clin. Cancer Res. *26*, 487–504. https://doi.org/10.1158/1078-0432.CCR-19-1868.
28. Boiarsky, R., Haradhvala, N.J., Alberge, J.B., Sklavenitis-Pistofidis, R., Mouhieddine, T.H., Zavidij, O., Shih, M.C., Firer, D., Miller, M., El-Khoury, H., et al. (2022). Single cell characterization of myeloma and its precursor conditions reveals transcriptional signatures of early tumorigenesis. Nat. Commun. *13*, 7040. https://doi.org/10.1038/s41467-022-33944-z.
29. Gai, D., Chen, J.R., Stewart, J.P., Nookaew, I., Habelhah, H., Ashby, C., Sun, F., Cheng, Y., Li, C., Xu, H., et al. (2022). CST6 suppresses osteolytic bone disease in multiple myeloma by blocking osteoclast differentiation. J. Clin. Invest. *132*, e159527. https://doi.org/10.1172/JCI159527.
30. Oliveira, C.S., de Bock, C.E., Molloy, T.J., Sadeqzadeh, E., Geng, X.Y., Hersey, P., Zhang, X.D., and Thorne, R.F. (2014). Macrophage migration inhibitory factor engages PI3K/Akt signalling and is a prognostic factor in metastatic melanoma. BMC Cancer *14*, 630. https://doi.org/10.1186/1471-2407-14-630.
31. Chen, R., Kang, R., and Tang, D. (2022). The mechanism of HMGB1 secretion and release. Exp. Mol. Med. *54*, 91–102. https://doi.org/10.1038/s12276-022-00736-w.
32. Zhan, F., Huang, Y., Colla, S., Stewart, J.P., Hanamura, I., Gupta, S., Epstein, J., Yaccoby, S., Sawyer, J., Burington, B., et al. (2006). The molecular classification of multiple myeloma. Blood *108*, 2020–2028. https://doi.org/10.1182/blood-2005-11-013458.
33. Danziger, S.A., McConnell, M., Gockley, J., Young, M.H., Rosenthal, A., Schmitz, F., Reiss, D.J., Farmer, P., Alapat, D.V., Singh, A., et al. (2020). Bone marrow microenvironments that contribute to patient outcomes in newly diagnosed multiple myeloma: A cohort study of patients in the Total Therapy clinical trials. PLoS Med. *17*, e1003323. https://doi.org/10.1371/journal.pmed.1003323.
34. Costa, F., Vescovini, R., Marchica, V., Storti, P., Notarfranchi, L., Dalla Palma, B., Toscani, D., Burroughs-Garcia, J., Catarozzo, M.T., Sammarelli, G., and Giuliani, N. (2020). PD-L1/PD-1 Pattern of Expression Within the Bone Marrow Immune Microenvironment in Smoldering Myeloma and Active Multiple Myeloma Patients. Front. Immunol. *11*, 613007. https://doi.org/10.3389/fimmu.2020.613007.
35. Sharma, A., Khan, R., Joshi, S., Kumar, L., and Sharma, M. (2010). Dysregulation in T helper 1/T helper 2 cytokine ratios in patients with multiple myeloma. Leuk. Lymphoma *51*, 920–927. https://doi.org/10.3109/10428191003699563.
36. Botta, C., Di Martino, M.T., Ciliberto, D., Cucè, M., Correale, P., Rossi, M., Tagliaferri, P., and Tassone, P. (2016). A gene expression inflammatory signature specifically predicts multiple myeloma evolution and patients survival. Blood Cancer J. *6*, e511. https://doi.org/10.1038/bcj.2016.118.
37. Schinke, C., Poos, A.M., Bauer, M., John, L., Johnson, S., Deshpande, S., Carrillo, L., Alapat, D., Rasche, L., Thanendrarajan, S., et al. (2022). Characterizing the role of the immune microenvironment in multiple myeloma progression at a single-cell level. Blood Adv. *6*, 5873–5883. https://doi.org/10.1182/bloodadvances.2022007217.
38. Dahlhoff, J., Manz, H., Steinfatt, T., Delgado-Tascon, J., Seebacher, E., Schneider, T., Wilnit, A., Mokhtari, Z., Tabares, P., Böckle, D., et al. (2022). Transient regulatory T-cell targeting triggers immune control of multiple myeloma and prevents disease progression. Leukemia *36*, 790–800. https://doi.org/10.1038/s41375-021-01422-y.
39. Lesokhin, A.M., Ansell, S.M., Armand, P., Scott, E.C., Halwani, A., Gutierrez, M., Millenson, M.M., Cohen, A.D., Schuster, S.J., Lebovic, D., et al. (2016). Nivolumab in Patients With Relapsed or Refractory Hematologic Malignancy: Preliminary Results of a Phase Ib Study. J. Clin. Oncol. *34*, 2698–2704. https://doi.org/10.1200/JCO.2015.65.9789.
40. Pianko, M.J., Funt, S.A., Page, D.B., Cattry, D., Scott, E.C., Ansell, S.M., Borrello, I.M., Gutierrez, M., Lendvai, N., Hassoun, H., et al. (2018). Efficacy and toxicity of therapy immediately after treatment with nivolumab

in relapsed multiple myeloma. Leuk. Lymphoma *59*, 221–224. https://doi.org/10.1080/10428194.2017.1320713.

41. Garon, E.B., Rizvi, N.A., Hui, R., Leighl, N., Balmanoukian, A.S., Eder, J.P., Patnaik, A., Aggarwal, C., Gubens, M., Horn, L., et al. (2015). Pembrolizumab for the treatment of non-small-cell lung cancer. N. Engl. J. Med. *372*, 2018–2028. https://doi.org/10.1056/NEJMoa1501824.
42. Badros, A., Hyjek, E., Ma, N., Lesokhin, A., Dogan, A., Rapoport, A.P., Kocoglu, M., Lederer, E., Philip, S., Milliron, T., et al. (2017). Pembrolizumab, pomalidomide, and low-dose dexamethasone for relapsed/refractory multiple myeloma. Blood *130*, 1189–1197. https://doi.org/10.1182/blood-2017-03-775122.
43. Mateos, M.V., Orlowski, R.Z., Ocio, E.M., Rodríguez-Otero, P., Reece, D., Moreau, P., Munshi, N., Avigan, D.E., Siegel, D.S., Ghori, R., et al. (2019). Pembrolizumab combined with lenalidomide and low-dose dexamethasone for relapsed or refractory multiple myeloma: phase I KEYNOTE-023 study. Br. J. Haematol. *186*, e117–e121. https://doi.org/10.1111/bjh.15946.
44. Mateos, M.V., Blacklock, H., Schjesvold, F., Oriol, A., Simpson, D., George, A., Goldschmidt, H., Larocca, A., Chanan-Khan, A., Sherbenou, D., et al. (2019). Pembrolizumab plus pomalidomide and dexamethasone for patients with relapsed or refractory multiple myeloma (KEYNOTE-183): a randomised, open-label, phase 3 trial. Lancet. Haematol. *6*, e459–e469. https://doi.org/10.1016/S2352-3026(19)30110-3.
45. Lonial, S., Richardson, P.G., Reece, D.E., Mohamed, H., Shelat, S., and San Miguel, J. (2017). CheckMate 602: An open-label, randomized, phase 3 trial of combinations of nivolumab, elotuzumab, pomalidomide and dexamethasone in relapsed/refractory multiple myeloma. J. Clin. Oncol. *35*, TPS8052. https://doi.org/10.1200/JCO.2017.35.15_suppl.TPS8052.
46. Usmani, S.Z., Schjesvold, F., Oriol, A., Karlin, L., Cavo, M., Rifkin, R.M., Yimer, H.A., LeBlanc, R., Takezako, N., McCroskey, R.D., et al. (2019). Pembrolizumab plus lenalidomide and dexamethasone for patients with treatment-naive multiple myeloma (KEYNOTE-185): a randomised, open-label, phase 3 trial. Lancet. Haematol. *6*, e448–e458. https://doi.org/10.1016/S2352-3026(19)30109-7.
47. Liu, J., Hamrouni, A., Wolowiec, D., Coiteux, V., Kuliczkowski, K., Hetuin, D., Saudemont, A., and Quesnel, B. (2007). Plasma cells from multiple myeloma patients express B7-H1 (PD-L1) and increase expression after stimulation with IFN-{gamma} and TLR ligands via a MyD88-TRAF6-and MEK-dependent pathway. Blood *110*, 296–304. https://doi.org/10.1182/blood-2006-10-051482.
48. Iwasa, M., Harada, T., Oda, A., Bat-Erdene, A., Teramachi, J., Tenshin, H., Ashtar, M., Oura, M., Sogabe, K., Udaka, K., et al. (2019). PD-L1 upregulation in myeloma cells by panobinostat in combination with interferon-gamma. Oncotarget *10*, 1903–1917. https://doi.org/10.18632/oncotarget.26726.
49. Cho, S.F., Anderson, K.C., and Tai, Y.T. (2022). Microenvironment Is a Key Determinant of Immune Checkpoint Inhibitor Response. Clin. Cancer Res. *28*, 1479–1481. https://doi.org/10.1158/1078-0432.CCR-22-0015.
50. Cristescu, R., Nebozhyn, M., Zhang, C., Albright, A., Kobie, J., Huang, L., Zhao, Q., Wang, A., Ma, H., Alexander Cao, Z., et al. (2022). Transcriptomic Determinants of Response to Pembrolizumab Monotherapy across Solid Tumor Types. Clin. Cancer Res. *28*, 1680–1689. https://doi.org/10.1158/1078-0432.CCR-21-3329.
51. Tamura, H., Ishibashi, M., Yamashita, T., Tanosaki, S., Okuyama, N., Kondo, A., Hyodo, H., Shinya, E., Takahashi, H., Dong, H., et al. (2013). Marrow stromal cells induce B7-H1 expression on myeloma cells, generating aggressive characteristics in multiple myeloma. Leukemia *27*, 464–472. https://doi.org/10.1038/leu.2012.213.
52. Liu, H., Kuang, X., Zhang, Y., Ye, Y., Li, J., Liang, L., Xie, Z., Weng, L., Guo, J., Li, H., et al. (2020). ADORA1 Inhibition Promotes Tumor Immune Evasion by Regulating the ATF3-PD-L1 Axis. Cancer Cell *37*, 324–339.e8. https://doi.org/10.1016/j.ccell.2020.02.006.
53. Garrett, I.R., Dallas, S., Radl, J., and Mundy, G.R. (1997). A murine model of human myeloma bone disease. Bone *20*, 515–520. https://doi.org/10.1016/s8756-3282(97)00056-2.
54. Chesi, M., Matthews, G.M., Garbitt, V.M., Palmer, S.E., Shortt, J., Lefebure, M., Stewart, A.K., Johnstone, R.W., and Bergsagel, P.L. (2012). Drug response in a genetically engineered mouse model of multiple myeloma is predictive of clinical efficacy. Blood *120*, 376–385. https://doi.org/10.1182/blood-2012-02-412783.
55. Stuart, T., Butler, A., Hoffman, P., Hafemeister, C., Papalexi, E., Mauck, W.M., 3rd, Hao, Y., Stoeckius, M., Smibert, P., and Satija, R. (2019). Comprehensive Integration of Single-Cell Data. Cell *177*, 1888–1902.e21. https://doi.org/10.1016/j.cell.2019.05.031.
56. Subelj, L., and Bajec, M. (2011). Unfolding communities in large complex networks: combining defensive and offensive label propagation for core extraction. Phys. Rev. E - Stat. Nonlinear Soft Matter Phys. *83*, 036103. https://doi.org/10.1103/PhysRevE.83.036103.
57. Finak, G., McDavid, A., Yajima, M., Deng, J., Gersuk, V., Shalek, A.K., Slichter, C.K., Miller, H.W., McElrath, M.J., Prlic, M., et al. (2015). MAST: a flexible statistical framework for assessing transcriptional changes and characterizing heterogeneity in single-cell RNA sequencing data. Genome Biol. *16*, 278. https://doi.org/10.1186/s13059-015-0844-5.
58. Bagwell, C.B., Inokuma, M., Hunsberger, B., Herbert, D., Bray, C., Hill, B., Stelzer, G., Li, S., Kollipara, A., Ornatsky, O., and Baranov, V. (2020). Automated Data Cleanup for Mass Cytometry. Cytometry A. *97*, 184–198. https://doi.org/10.1002/cyto.a.23926.

STAR★METHODS

KEY RESOURCES TABLE

REAGENT or RESOURCE	SOURCE	IDENTIFIER
Antibodies		
FITC anti-mouse/human CD45R/B220 Antibody	Biolegend	Cat# 103206; RRID: AB_312991
BV786 Rat Anti-Mouse CD25	BD Biosciences	Cat# 564368; RRID: AB_2738771
PE anti-mouse CD117 (c-Kit) Antibody	Biolegend	Cat# 105808; RRID: AB_313217
PE/Cyanine7 anti-mouse IgM Antibody	Biolegend	Cat# 406514; RRID: AB_10642031
CD274 (PD-L1, B7-H1) Monoclonal Antibody (MIH5), APC	Thermo Fisher	Cat# 17-5982-82; RRID: AB_2688092
FITC anti-mouse CD62L Antibody	Biolegend	Cat# 104406; RRID: AB_313093
PE anti-mouse CD8a Antibody	Biolegend	Cat# 100708; RRID: AB_312747
PE/Cyanine7 anti-mouse CD4 Antibody	Biolegend	Cat# 100422; RRID: AB_312707
BV786 Rat Anti-Mouse CD44	BD Biosciences	Cat# 563736; RRID: AB_2738395
APC anti-mouse CD279 (PD-1) Antibody	Biolegend	Cat# 135209; RRID: AB_2251944
PE anti-mouse CD138 (Syndecan-1) Antibody	Biolegend	Cat# 142504; RRID: AB_10916119
CD19 Monoclonal Antibody (eBio1D3 (1D3)), eFluor^{TM} 450	Thermo Fisher	Cat# 48-0193-82; RRID: AB_2734905
CD11b Monoclonal Antibody (M1/70), FITC	Thermo Fisher	Cat# 11-0112-85; RRID: AB_464936
PerCP anti-mouse CD11c Antibody	Biolegend	Cat# 117326; RRID: AB_2129643
BV786 Rat Anti-Mouse Ly-6G	BD Biosciences	Cat# 740953; RRID: AB_2740578
PE/Cyanine7 anti-mouse Ly-6C Antibody	Biolegend	Cat# 128018; RRID: AB_1732082
Brilliant Violet 605^{TM} anti-mouse F4/80 Antibody	Biolegend	Cat# 123133; RRID: AB_2562305
APC anti-mouse CD274 (B7-H1, PD-L1) Antibody	Biolegend	Cat# 124312; RRID: AB_10612741
CD3e Monoclonal Antibody (145-2C11), APC-eFluor 780	Thermo Fisher	Cat# 47-0031-82; RRID: AB_11149861
Granzyme B Monoclonal Antibody (NGZB), APC	Thermo Fisher	Cat# 17-8898-82; RRID: AB_2688068
IFN gamma Monoclonal Antibody (XMG1.2), PE-Cyanine7	Thermo Fisher	Cat# 25-7311-82; RRID: AB_469680
CD4 Monoclonal Antibody (GK1.5), eFluor 450	Thermo Fisher	Cat# 48-0041-82; RRID: AB_10718983
PerCP Rat Anti-Mouse CD8a	BD Biosciences	Cat# 553036; RRID: AB_394573
PE anti-mouse CD279 (PD-1) Antibody	Biolegend	Cat# 135205; RRID: AB_1877232
NK1.1 Monoclonal Antibody (PK136), Super Bright^{TM} 600	Thermo Fisher	Cat# 63-5941-82; RRID: AB_2637451
TruStain FcX^{TM} (anti-mouse CD16/32) Antibody	Biolegend	Cat# 101320; RRID: AB_1574975
Human TruStain FcX^{TM}	Biolegend	Cat# 422302; RRID: AB_2818986
APC anti-human CD14 Antibody	Biolegend	Cat# 301808; RRID: AB_314190
APC/Cyanine7 anti-human CD45 Antibody	Biolegend	Cat# 304014; RRID: AB_314402
FITC anti-human CD138 (Syndecan-1) Antibody	Biolegend	Cat# 352304; RRID: AB_10900441
PE anti-human CD274 (B7-H1, PD-L1) Antibody	Biolegend	Cat# 329706; RRID: AB_940368
FITC anti-human CD279 (PD-1) Antibody	Biolegend	Cat# 329904; RRID: AB_940479
PE anti-human CD4 Antibody	Biolegend	Cat# 357404; RRID: AB_2562036
APC anti-human CD8 Antibody	Biolegend	Cat# 344722; RRID: AB_2075388
APC/Cyanine7 anti-human CD3 Antibody	Biolegend	Cat# 300318; RRID: AB_314054
Nek2 Antibody (D-8)	Santa Cruz	Cat# sc-55601; RRID: AB_1126558
GAPDH Antibody (6C5)	Santa Cruz	Cat# sc-32233; RRID: AB_627679
Phospho-Jak1(Tyr1034/1035) (D7N4Z) Rabbit mAb	Cell Signaling	Cat# 74129; RRID: AB_2799851
Jak1 Antibody	Cell Signaling	Cat# 3332; RRID: AB_2128499
Phospho-Jak2 (Tyr1007/1008) Antibody	Cell Signaling	Cat# 3771; RRID: AB_330403
Jak2 (D2E12) XP® Rabbit mAb	Cell Signaling	Cat# 3230; RRID: AB_2128522
Phospho-Stat1 (Tyr701) (D4A7) Rabbit mAb	Cell Signaling	Cat# 7649; RRID: AB_10950970
Stat1 (D1K9Y)	Cell Signaling	Cat# 14994; RRID: AB_2737027

(*Continued on next page*)

Continued

REAGENT or RESOURCE	SOURCE	IDENTIFIER
IRF-1 (D5E4) XP®	Cell Signaling	Cat# 8478; RRID: AB_10949108
PD-L1 (D4H1Z)	Cell Signaling	Cat# 60475; RRID: AB_2924680
β-Tubulin Antibody	Cell Signaling	Cat# 2146; RRID: AB_2210545
Arginase-1 (D4E3M^{TM}) XP® Rabbit mAb	Cell Signaling	Cat# 93668; RRID: AB_2800207
C/EBPβ (LAP) Antibody	Cell Signaling	Cat# 3087; RRID: AB_2078052
PI3 Kinase Antibody Sampler Kit	Cell Signaling	Cat# 9655; RRID: AB_1642274
Phospho-Akt (Ser473) (D9E) XP® Rabbit mAb	Cell Signaling	Cat# 4060; RRID: AB_2315049
Phospho-Akt (Thr308) (D25E6) XP® Rabbit mAb	Cell Signaling	Cat# 13038; RRID: AB_2629447
Akt (pan) (C67E7) Rabbit mAb	Cell Signaling	Cat# 4691; RRID: AB_915783
Phospho-Stat3 (Tyr705) (D3A7) XP® Rabbit mAb	Cell Signaling	Cat# 9145; RRID: AB_2491009
Stat3 (79D7) Rabbit mAb	Cell Signaling	Cat# 4904; RRID: AB_331269
PDL1 (7310) Bond RTU Primary	Leica Biosystems	Cat# PA0832; RRID: AB_2934049
Purified anti-mouse CD3ε Antibody	Biolegend	Cat# 100302; RRID: AB_312667
InVivoPlus anti-mouse PD-L1 (B7-H1) (Clone 10F.9G2)	Bio X Cell	Cat# BP0101; RRID: AB_2934050
InVivoMAb anti-human PD-L1 (B7-H1) (Clone 29E.2A3)	Bio X Cell	Cat# BE0285; RRID: AB_2687808
Biological samples		
Bone marrow specimens (FFPE) from myeloma patients	Institute of Pathology, UAMS	N/A
Bone marrow mononuclear cells (BM-MNCs) from myeloma patients	Tissue Biorepository and Procurement Core, UAMS	N/A
Chemicals, peptides, and recombinant proteins		
INH154	MedChem Express	HY-117154
4x Laemmli sample buffer	Bio-Rad	161–0747
Restore^{TM} PLUS Western Blot Stripping Buffer	Thermo Fisher	46430
Western ECL Substrate	Bio-Rad	170–5060
Recombinant Murine M-CSF	PeproTech	315-02-50UG
Mouse GM-CSF	Thermo Fisher	50-925-6
CellTrace^{TM} Violet	Thermo Fisher	C10094
7-AAD	Biolegend	420404
2-mercaptoethanol	Thermo Fisher	21985023
Monensin Solution	Thermo Fisher	00-4505-51
Brefeldin A Solution	Thermo Fisher	00-4506-51
Cell Stimulation Cocktail	Thermo Fisher	50-930-5
Critical commercial assays		
Molecular Probes PrestoBlue^{TM} Cell Viability Reagent	Thermo Fisher	A13261
Tali^{TM} Cell Cycle Solution	Thermo Fisher	A10798
LIVE/DEAD^{TM} Fixable Aqua Dead Cell Stain Kit	Thermo Fisher	L34965
Foxp3/Transcription Factor Staining Buffer Set	Thermo Fisher	50-112-8857
CD19 MicroBeads, mouse	Miltenyi Biotec	130-121-301
CD11b MicroBeads, mouse and human	Miltenyi Biotec	130-049-601
CD3e MicroBead kit, mouse	Miltenyi Biotec	130-094-973
CD8a+ T cell Isolation Kit, mouse	Miltenyi Biotec	130-104-075
CD8 MicroBeads human	Miltenyi Biotec	130-045-201
Dynabeads^{TM} Mouse T-Activator CD3/CD28 for T cell Expansion and Activation	Thermo Fisher	11-456-D
Dynabeads^{TM} Human T-Activator CD3/CD28 for T cell Expansion and Activation	Thermo Fisher	11-131-D
Mammalian Cell & Tissue Extraction Kit	BioVision	K269-500
BCA Protein Assay Kit	Thermo Fisher	23225
Mouse IFN-gamma Quantikine ELISA Kit	R&D	MIF00

(Continued on next page)

Continued

REAGENT or RESOURCE	SOURCE	IDENTIFIER
Mouse IgG2b ELISA Quantitation Set	Bethy Laboratories	E90-109
QuickGel SPE Kit	Helena	3505T
Cytometric Bead Array (CBA) Human Th1/Th2 Cytokine Kit II	BD Biosciences	551809
RNeasy Plus Kit	QIAGEN	74034
iScript$^{\text{TM}}$ Reverse Transcription Supermix	Bio-Rad	1708841
iTaq$^{\text{TM}}$ Universal SYBR® Green Supermix	Bio-Rad	1725121
Deposited data		
RNA-seq data on spleen B cells of Eμ-*myc* mice	This paper	GEO: GSE226675
Single-cell RNA seq data on BM cells of 5TGM1 MM mouse model	This paper	GEO: GSE226697
GitHub	Kenneth Hu Github	https://doi.org/10.5281/zenodo.7697398 https://doi.org/10.5281/zenodo.7702421
Experimental models: Cell lines		
5TGM1 MM	Harlan Laboratory Inc.	Garrett et al.[53]
Vκ12653 MM	Mayo Clinic	Chesi et al.[54]
Experimental models: Organisms/strains		
MOUSE: B6. *Nek2*$^{-/-}$	Mutant Mouse Resource & Research Centers	https://www.mmrrc.org/catalog/sds.php?mmrrc_id=48780
MOUSE: Eμ-*myc*	The Jackson Laboratory	https://www.jax.org/strain/002728
MOUSE: C57BL/6J	The Jackson Laboratory	https://www.jax.org/strain/000664
MOUSE: C57BL/KalwRijHsd	The Harlan Laboratory	https://www.envigo.com/model/c57bl-kalwrijhsd
Oligonucleotides		
Primer: *Nek2* wild type allele Forward: CAA CAT GAC ACC ATG GAA AAC CG and Reverse: GAG CAT GAG GAC CAG AAA ACG ATG G	This paper	N/A
Primer: *Nek2* knockout allele Forward primer GAG ATG GCG CAA CGC AAT TAA T and reverse primer TTT GGT TGA AAG CTG TAA AGG GAG GC	This paper	N/A
Primer: *NEK2* Forward: GGA TGG CAA GCA AAA CGT CA and Reverse: TAC AGC AAG CAG CCC AAT GA	This paper	N/A
Primer: *ACTB* Forward: GGG CAT GGG TCA GAA GGA TT and Reverse: TCG ATG GGG TAC TTC AGG GT	This paper	N/A
Software and algorithms		
FlowJo_V10	BD Biosciences	https://www.flowjo.com/solutions/flowjo
GraphPad Prism 9	Graph Pad	https://www.graphpad.com
ImageJ	ImageJ	https://imagej.nih.gov/ij/download.html
Image Lab 6.1	Bio-Rad	https://www.bio-rad.com/en-us/product/image-lab-software?ID=KRE6P5E8Z
OsteoMeasure 7.0	Osteometrics, Inc.	https://www.osteometrics.com/HRCVS.htm
ImageScope	Leica Biosystems	https://www.leicabiosystems.com/us/digital-pathology/manage/aperio-imagescope/
GO and KEGG analyses	ShinyGO 0.76.3	http://bioinformatics.sdstate.edu/go/
Cytobank	Beckman Coulter, Inc	https://premium.cytobank.org/cytobank/login

RESOURCE AVAILABILITY

Lead contact

Further information and requests for resources and reagents should be directed to and will be fulfilled by the lead contact, Fenghuang Zhan (fzhan@uams.edu).

Materials availability

This study did not generate new unique reagents.

Data and code availability

Bulk RNA-seq and single cell RNA-seq data have been deposited at the Gene Expression Omnibus GEO: GSE226675 and GEO: GSE226697. Gene expression profiling data from human CD138$^+$ MM cells are available under GEO: GSE19554, GEO: GSE2658 and GEO: GSE19784. All original code has been deposited to GitHub. DOIs are listed in the key resource table. Any additional information required to reanalyze the data reported in this paper is available from the lead contact upon request.

EXPERIMENTAL MODEL AND STUDY PARTICIPANT DETAILS

Mice

Eμ-myc strain (JAX stock# 002728) and C57BL/6J strain (JAX stock# 000664) mice were purchased from Jackson Laboratories. C57BL/KaLwRij mice were obtained from Harlan Laboratory Inc. (Harlan Mice, Netherlands). *Nek2*$^{-/-}$ mice were bred to C57BL/KaLwRij background for 10 generations for 5TGM1 MM transfer experiments. All mice were bred and maintained at the University of Arkansas for Medical Sciences (UAMS) Animal Facility on a 12-h light/dark cycle with stable temperature (22°C) and humidity (60%) with free access to food and water. 8–10 weeks half male and half female mice were used for experimentations unless otherwise indicated. All animal procedures were conducted under the regulatory standards approved by the UAMS Institution of Institutional Animal Care and Use Committee (Protocol #3991).

Generation of *Nek2* knockout mice

Three embryonic stem (ES) clones Nek2_B10, Nek2_F10 and Nek2_G11 with *Nek2* disruption cassettes were purchased from Mutant Mouse Resource & Research Centers. The original allele for this mutation is of type 'Knockout-First - Reporter Tagged Insertion'. The three ES clones were injected into pseudo-pregnant C57BL6 mice and *Nek2* knockout mice were generated by gene trap and CMV-Cre. Primers for identification of *Nek2* wild type allele are forward primer 5′-CAA CAT GAC ACC ATG GAA AAC CG-3′ and reverse primer 5′-GAG CAT GAG GAC CAG AAA ACG ATG G-3'. Primers for identification of the knockout allele are forward primer 5′-GAG ATG GCG CAA CGC AAT TAA T-3′ and reverse primer 5′-TTT GGT TGA AAG CTG TAA AGG GAG GC-3'.

Pre-tumoral analysis of Eμ-myc model

Eμ-myc mice were crossed with *Nek2* knockout mice. The offspring harboring Eμ-myc transgenes and *Nek2* knockout allele were genotyped by polymerase chain reaction (PCR) respectively. Primers for identification of Eμ-myc transgenes are forward primer 5′- TTA GAC GTC AGG TGG CAC TT-3′ and reverse primer 5′-TGA GCA AAA ACA GGA AGG CA-3'. To monitor mouse survival, Eμ-myc mice with different *Nek2* genotyping (*Nek2*$^{-/-}$, *Nek2*$^{+/-}$, *Nek2*$^{+/+}$) were sacrificed upon the development of advanced diseases such as visible or palpable lumps, a hunched posture, tachypnea, a swollen belly, or ruffled fur. To study pre-tumoral cell biology, we collected peripheral blood, spleen, thymus, and bone marrow at 6–8 weeks of age for further analysis. Peripheral blood was collected into an EDTA tube followed by a complete blood count (CBC) determined with Vetscan HM5 Hematological analyzer (Zoetis). Spleen and thymus were weighted, and single cell suspension was obtained by squeezing and filtering through a sterile 70 μm cell strainer (BD Falcon). Bone marrow cells were obtained by flushing with a 1 mL syringe with a 25-gauge needle. Red blood cells were lysed, and cells were washed twice with PBS buffer before continuing with flow cytometry or magnetic-activated cell sorting (MACS).

Transplantable multiple myeloma mouse models

Transplantable 5TGM1 MM cell line[53] and Vκ12653 MM cell line[54] were generated and expanded as previously described. 5TGM1 (1×10^6) or Vκ12653 (1×10^6) were injected i.v. via tail vein of C57BL/KaLwRij mice and C57BL/6J mice, respectively. Mouse serum was obtained by submandibular blood sampling. Serum IgG2b or M-protein levels were detected by ELISA or electrophoresis, respectively. Mouse BM and spleen cells were harvested and the percentage of CD19$^-$CD138$^+$ plasma cells was analyzed by flow cytometry at indicated time points. For survival analysis, mice were monitored daily and were euthanized when mice developed signs of reduced mobility including paralysis, hunched posture, or respiratory distress.

METHOD DETAILS

In vivo treatment

The NEK2 inhibitor INH154 was gifted from the Bipharm and dissolved in the solvent 10% DMSO, 40% PEG300, 5% Tween-80, and 45% saline and given at 10 mg/kg i.p. twice a week. PD-L1 mAb (Clone 10F.9G2, Bio X Cell) was given at 100 μg/mouse/100 μL i.p. twice a week. The vehicle groups were given by the solvent at the same frequency.

Mouse serum protein electrophoresis

Mouse serum protein electrophoresis was performed using Helena QuickGel Electrophoresis system followed by the manufacture's instruction. Briefly, mouse serum was diluted with saline at 1:4 ratio. One μL of diluted samples was loaded to the gel and electrophoresis for 5 min and 45 s. Gel was stained with Comassie Blue and destained with acetic acid and methanol before drying. Vk12653 tumor bearing mice show a predominant monoclonal gamma banding in the gamma region. The quantification of the percentage of γ-globulin was analyzed by ImageJ.

Flow cytometry

Single cell suspensions were pre-incubated with anti-mouse CD16/32 antibody (Biolegend) for 30 min for blocking prior to labeling with fluorochrome-conjugated antibodies for 30 min at 4°C. For intracellular antibody staining, freshly isolated cells were incubated with Monensin solution (Thermo Fisher), Brefeldin A solution (Thermo Fisher) and Cell stimulation cocktail (Thermo Fisher), for 4 h. After being stained with surface antibodies, cells were fixed in 4% paraformaldehyde for 10 min, following fixation permeabilize the cells by adding 500 μL of Fix/Perm buffer (Thermo Fisher) overnight. The next day, cells were washed with Perm buffer and incubated with an intracellular antibody cocktail for 30 min at 4°C. Cells were washed twice with perm buffer and once in fluorescence-activated cell sorting (FACS) buffer prior to running. Data acquisition was performed using BD FACSverse, Celesta or LSRFortessa Flow Cytometer (BD Biosciences). Raw data were analyzed using FlowJo software for visualization and quantification.

Bulk RNA sequence

$CD19^+$ B cells from Eμ-myc mice with or without *Nek2* knockout were isolated from spleen by MACS and were processed for RNA extraction using RNeasy Plus mini kit (74134, Qiagen). RNA concentration and purity were determined on NanoDrop. Deep RNA sequence was conducted at the Genomics Division of the Iowa Institute of Human Genetics.

Single cell RNA sequence (scRNA-seq)

Bone marrow cells were harvested and counted using a fluorescence microscope. Samples with viability higher than 95% were processed for 10x genomics scRNA-seq. Approximately 10,000 cells were targeted, and single-cell emulsions were generated with the Chromium Controller (10x Genomics, Pleasanton, CA, USA) using the Chromium Next GEM Chip G (Part Number 1000120, 10x Genomics) with the Chromium NextGEM Single Cell 3′ v3.1 kit (Part Number 1000121, 10x Genomics) following the standard protocol. Libraries were assessed for mass concentration using the Qubit 1X dsDNA HS Assay Kit (catalog #Q33231; Invitrogen, Waltham MA, USA) and the Qubit 4 fluorometer (catalog #Q33238; Invitrogen, Waltham MA, USA). Library fragment size was assessed with the High Sensitivity NGS Fragment Analysis Kit (catalog # DNF-474-0500; Agilent, Santa Clara CA, USA) on the Fragment Analyzer System (catalog #M5310AA; Agilent, Santa Clara CA, USA). Libraries were functionally validated with the KAPA Universal Library Quantification Kit (catalog # 07960140001; Roche, Basel CH). Initial low-pass "surveillance" sequencing was performed on an Illumina NovaSeq SP 100-cycle flow cell and data were assessed using the Cell Ranger Count output.

Bioinformatics analysis

Raw scRNA-seq data were preprocessed using the Cell Ranger analysis pipelines (10x Genomics) version 6 with reference genome of Mus musculus version mm10 to demultiplex for cell and transcript and generate count table. The count table was loaded into R through Seurat version 4 package[55] for further analysis. Cells that have gene numbers lesser than 200, greater than 7,000, and more than 10% of unique molecular identifiers stemming from mitochondrial genes were discarded from the analysis. For individual sample, a principal component analysis (PCA) was performed on significantly variable genes for remained high-quality cells. Results of individual samples were used for data integration across samples using reciprocal PCA method to minimize technical differences between samples. The integration results were employed as input for clustering using Louvain algorithm with multilevel refinement[56] and the Uniform Manifold Approximation and Projection for Dimension Reduction (UMAP). Expression patterns of selected marker genes across cell clusters were plotted as a heatmap to assess the quality of cell clustering. After quality control, we obtained high quality single-cell transcriptomes average 7,600 cells per sample. Cell types were assigned using followings gene markers: *Sdc1* (MM cells), *Cd74*, *H2Ab1* (Pre-B cells), *Vpreb3*, *Akap12* (Pro-B cells), *Gzma*, *Klra4*, *Cd3d*, *Cd3e* (NK and T cells), *Itgax*, *Siglech* (DCs), *Elane*, *Mpo*, *Ctsg*, *Ms4a3* (Myeloblasts), *Fcnb*, *Ltf*, *Lcn2* (Myelocytes), *Ly6g*, *Mmp8*, *Cxcr2* (Neutrophils), *F13a1*, *Irf8*, *Ly86* (Monoblasts), *S100a4*, *Pld4*, *Csf1r* (Monocytes), and *Adgre1* (Macrophages). The gene-specific markers of each cluster were identified using Seurat's FindAllMarkers function with the Model-based Analysis of Single Cell Transcriptomics (MAST) package.[57] To analyze heterogeneity of Macrophages and NK/T population, we selected each cluster and performed subcluster analysis using the Seurat's FindClusters function. GO and KEGG analyses were performed by ShinyGO 0.76.3 and enriched signaling pathways were selected by a false discovery rate cutoff 0.05 and sorted by the fold enrichment.

Micro-computed tomography (μCT)

Mouse tibiae were fixed in 10% neutral-buffered formalin for 2 days μCT was performed using SkyScan1272 scanner (Bruke) with the following settings: 60 kV and 166 μA, Al 0.5 mm filter,10 μM pixel size. Images were reconstructed using the Skyscan NRecon program (version 2.0) with a beam-hardening correction of 40. Trabecular and cortical bone microarchitecture were analyzed using the Skyscan CT Analyzer program (version 2.0). Osteolytic lesions on the curved medial tibial surface that completely penetrated the cortical bone and were greater than 100 μm in diameter were counted.

Bone histomorphometry

Mouse tibiae were fixed in 10% neutral-buffered formalin for 2 days, decalcified in 5% EDTA solution (pH 7.0) for 7 days, dehydrated and embedded in paraffin. Bone sections were cut at 5 μm thickness and stained with H&E and TRAP using a Leukocyte Acid Phosphatase Kit (Sigma-Aldrich). Histomorphometric analyses were performed using OsteoMeasure software (OsteoMetrics, version 7.0), with a Zeiss Axioskop2 microscope (Carl Zeiss).

In vitro TAMs and MDSCs generation

Bone marrow cells collected from *Nek2*$^{+/+}$ or *Nek2*$^{-/-}$ mice were isolated from femur and tibia and cultured in Dulbecco modified Eagle medium (Gibco) containing 10% fetal calf serum, 2 mM glutamine, 100 U/ml penicillin, 100 mg/mL streptomycin, and 50 mM 2-mercaptoethanol. M-CSF (10 ng/mL, Biolegend) or GM-CSF (10 ng/mL, Biolegend) was added to induce macrophages (6 days) or MDSCs (4 days), respectively. 5TGM1 conditioned media were added for additional 2 days to induce TAMs. In some experiments, mouse CD11b$^+$ cells were selected by MACS from freshly isolated bone marrow cells or cultured MDSCs for subsequent analyses.

Functional Assay of T Cells Co-cultured with TAMs or MDSCs

CD8$^+$ T cells were isolated from spleen by MACS using anti-CD8 microbeads, and stained with CellTrace Violet (CTV, Thermo Fisher) according to manufacturer's instruction. Isolated CD8$^+$ T cells were co-cultured with TAMs or MDSCs at 4:1 ratio on 96-well plates coated with anti-CD3 (2.5 mg/mL) for 72 h. The percentages of proliferating CD8$^+$ T cells were determined by CTV dilution assessment. IFN-γ levels in the culture supernatant were measured by ELISA (R&D).

Cell viability and cell cycle

Macrophage cell viability was detected by PrestoBlue Cell Viability Reagent (Thermo Fisher). Cell cycle progression was measured with the help of the Tali Cell Cycle Kit (Thermo Fisher). All experimental processes were conducted with manufactural instructions.

Western Blot

Proteins were harvested under instruction of Cell and Tissue Extraction Kit (K269-500, BioVision). Protein concentrations were determined using the Pierce BCA Protein Assay Kit (23225, Thermo). A total of 35 μg protein per sample was loaded and separated by SDS-PAGE (Thermo) and transferred to nitrocellulose membranes. After blocking with 5% skimmed milk, membranes were blotted with first antibodies followed by appropriated HRP-conjugated secondary antibodies. The proteins were visualized by enhanced chemiluminescence using ChemiDoc XRS+ System (Bio-Rad).

Isolation and Purification of human myeloma cells

All patients gave written informed consent and collection was approved by the UAMS review boards (IRB #261820). Fresh bone marrow aspirates from MM patients were collected at the time of diagnosis in the University of Arkansas for Medical Sciences and were diluted to 25 mL with PBS and overlaid on lymphocyte separation media (Corning). Following centrifugation, collected buffy coat was washed with PBS and resuspended in RPMI1640 medium, defined as bone marrow mononuclear cells (BM-MNCs). CD138$^+$ MM cells were purified using immunomagnetic bead selection with monoclonal mouse anti–human CD138 antibody with the use of the AutoMACS automated separation system (Miltenyi-Biotec). PC purity of >95% homogeneity was confirmed by 2-color flow cytometry with the use of CD138$^+$/CD45$^-$ criteria (Becton Dickinson), immunocytochemistry for cytoplasmic light-chain immunoglobulin, and morphology by Wright-Giemsa staining.

Gene expression profiling

RNA of CD138$^+$ MM cells was extracted using the RNeasy kit (Qiagen). cDNA was prepared and biotinylated with the Affymetrix GeneChip HT 3′ IVT Express Kit. Samples were hybridized to an Affymetrix Human Genome U133 Plus 2.0 Array Chip according to the manufacturer's recommendations and then read on a GeneChip Scanner 3000 System (Thermo Fisher).

Quantitative real-time PCR (qRT-PCR)

RNA of CD138$^+$ MM cells was extracted using the RNeasy Plus mini kit (74134, Qiagen). RNA concentration and purity were determined on NanoDrop. cDNA synthesis was conducted using the iScript reverse transcription kit (1708841, Bio-Rad). qRT-PCR was performed on the CFX Connect Real-Time System (Bio-Rad) using reagents of SYBR Green Supermix (1725121, Bio-Rad). Primer sequences of *NEK2* are forward primer 5′- GGA TGG CAA GCA AAA CGT CA-3′ and reverse primer 5′- TAC AGC AAG CAG CCC AAT GA-3’. Primer sequences of *ACTB* are forward primer 5′-GGG CAT GGG TCA GAA GGA TT-3′ and reverse primer 5′-TCG ATG GGG TAC TTC AGG GT-3’. mRNA levels were calculated using the $2^{-\Delta\Delta Ct}$ method and normalized to ACTB.

Functional Assays of human T cells

Freshly BM-MNCs were detected expression of PD1 on $CD8^+$ and $CD4^+$ T cells by flow cytometry. $CD138^-$ BM-MNCs or sorted $CD8^+$ T cells were stimulated with anti-CD3/CD28 microbeads (Thermo Fisher). Cytokine levels were measured in cell culture supernatants by Cytometric Bead Array (CBA) (BD Biosciences) after 24 h. Alternatively, cells were stained with CellTrace Violet (CTV, Thermo Fisher) before anti-CD3/CD28 microbead stimulation followed by CTV dilution assessment 5 days later.

Immunohistochemistry (IHC)

MM bone marrow biopsies were embedded in paraffin, sliced into 4 μm sections, and dried in 55°–60° oven for 30 min. NEK2 (D-8, sc-55601, Santa Cruz) and PD-L1 (PA0832, Leica biosystems) staining were performed on Leica BondRX IHC staining platform. Slide sections were pre-treated using heat-mediated antigen retrieval buffer for 30 min at 98°C. The section was then incubated with primary antibody, 5 μg/mL working concentration, for 60 min at room temperature and detected using an HRP conjugated compact polymer system for 8 min at room temperature. DAB was used as chromogen for 10 min at room temperature. The section was then counterstained with hematoxylin, blued, dehydrated, cleared, and mounted with DPX (Phthalate Free) mounting media. Representative images were captured and quantified using the ImageScope software (Leica Biosystems).

Mass cytometry (CyTOF)

Cryopreserved BM-MNCs were thawed, stained with metal-tagged antibodies, and acquired on a Helios mass cytometer (Standard BioTools Inc.) according to the manufacturer’s recommendation. Data were normalized using calibration beads and then uploaded to an online analysis tool, Cytobank, for further processing. Initial data clean-up was performed using the Gaussian parameters method as published previously.[58] Cleaned single cell events were gated for $CD38^+CD45^{-/dim}$ MM cells and $CD45^+$ immune cells, t-distributed stochastic neighbor embedding (t-SNE) and flow self-organizing map (FlowSOM) algorithms were implemented for dimensionality reduction and deep cell clustering.

In vitro treatment of primary BM-MNCs

1-2 × 10^6 fresh BM-MNCs were cultured *in vitro* and treated with either a NEK2 inhibitor INH154 (HY-117154, MCE) at 2 μM, blocking PD-L1 mAbs at 10 ng/mL (Clone 29E.2A3, Bio X Cell), or both for 24 h. Cells were harvested and stained for flow cytometry.

QUANTIFICATION AND STATISTICAL ANALYSIS

Statistical analyses were performed using the GraphPad Prism 9 Software. Unless indicated in the figure legends, results were expressed as Mean ± SD. Student’s *t* test was used for comparisons between two groups. For comparison of means among multiple groups in one factor or two factors, a one-way ANOVA followed by a Tukey’s multiple comparison test, or a two-way ANOVA followed by Sidak multiple comparison test were used respectively. Paired sample data were analyzed using randomized block (repeated measures) ANOVA followed by a Tukey’s multiple comparison test. Overall survival and disease-free survival curves were evaluated using the Kaplan-Meier method and compared using the log rank test. Statistical significances are indicated as follows in figures: $p < 0.001$ as ***, $p < 0.01$ as **, and $p < 0.05$ as *.